Earth-Science Reviews 226 (2022) 103916

Contents lists available at ScienceDirect

Earth-Science Reviews

journal homepage: www.elsevier.com/locate/earscirev

Laboratory experiments on fault behavior towards better understanding of injection-induced seismicity in geoenergy systems

Yinlin Ji [a,*], Hannes Hofmann [a], Kang Duan [b], Arno Zang [a]

[a] Helmholtz Centre Potsdam, GFZ German Research Centre for Geosciences, 14473 Potsdam, Germany
[b] School of Civil Engineering, Shandong University, 250061 Jinan, China

ARTICLE INFO

Keywords:
Shear-flow experiments
Fluid injection
Induced seismicity
Fault behavior
Fault reactivation
Injection protocol/strategy

ABSTRACT

Induced seismicity associated with fluid injection into underground formations jeopardizes the sustainable utilization of the subsurface. Understanding the fault behavior is the key to successful management and mitigation of injection-induced seismic risks. As a fundamental approach, laboratory experiments have been extensively conducted to assist constraining the processes that lead to and sustain various injection-induced fault slip modes. Here, we present a state-of-the-art review on the emerging topic of injection-induced seismicity from the laboratory perspective. The basics of fault behavior, including fault strength and instability, are first briefly summarized, followed by the paradoxical stability analysis arising from the current theoretical framework. After the description of common laboratory methods and auxiliary techniques, we then comprehensively review the effects of fault properties, stress state, temperature, fluid physics, fluid chemistry and injection protocol on fault behavior with particular focus on the implications for injection-induced seismicity. We find that most of the shear tests are conducted under displacement-driven conditions, while the number of injection-driven shear tests is comparatively limited. The review shows that the previous work on displacement-driven rock friction and fault slip modes partially unravel the mystery of injection-induced fault behavior, and recent experimental studies on the injection-driven response of critically stressed faults provide complementary insights. Overall, laboratory experiments have substantially advanced especially our understanding of the roles of fault roughness, fault mineralogy, stress state, fluid viscosity, fluid induced mineral dissolution, and injection rate in injection-induced seismicity, which has been successfully used to interpret many field observations. However, there are still outstanding questions in this area, which could be addressed by future experimental studies, such as the feasibility of seismic-informed adaptive injection strategy for mitigating seismic risks, colder fluid injection into critically stressed faults under hydrothermal conditions, and fault friction evolution during cyclic injection spanning from undrained to drained conditions.

List of abbreviations

AE	Acoustic emission
AFM	Atomic force microscope
EHD	Elasto-hydrodynamic
EGS	Enhanced geothermal systems
HiQuake	Human-Induced Earthquake Database
PMMA	Polymethyl methacrylate
RSF	Rate-and-state friction
SEM	Scanning electron microscope
XRD	X-ray powder diffraction

1. Introduction

The injection of pressurized fluids into underground formations is currently indispensable in many geo-energy applications. Nevertheless in the past decades, injection-induced seismicity has been frequently reported worldwide (Foulger et al., 2017), e.g., in enhanced geothermal systems (EGS) (Elsworth et al., 2016; Gaucher et al., 2015; Grigoli et al., 2018; Kim et al., 2018; Lee et al., 2019; Majer et al., 2007; Rathnaweera et al., 2020; Zang et al., 2014), in tight oil and gas reservoirs (e.g., Bao and Eaton, 2016; Lei et al., 2017a; Li et al., 2019), and in wastewater disposal (Ellsworth, 2013; Kolawole et al., 2019; Walsh and Zoback, 2015). More specifically, the 2017 M_w 5.5 earthquake that occurred in

* Corresponding author.
E-mail address: yinlinji@gfz-potsdam.de (Y. Ji).

https://doi.org/10.1016/j.earscirev.2021.103916
Received 26 July 2021; Received in revised form 29 October 2021; Accepted 31 December 2021
Available online 6 January 2022
0012-8252/© 2022 The Authors. Published by Elsevier B.V. This is an open access article under the CC BY-NC-ND license (http://creativecommons.org/licenses/by-nc-nd/4.0/).

Pohang, South Korea is attributed to fluid injection in the nearby EGS (Woo et al., 2019). The 2016 M_w 4.1 earthquake in Duvernay, western Canada results from hydraulic fracturing for shale gas extraction (Bao and Eaton, 2016). Several recent earthquakes in Oklahoma (e.g., the 2016 M_w 5.8 Pawnee earthquake and the 2016 M_w 5.1 Fairview earthquake), United States are caused by the disposal of wastewater from fracking operations (Kolawole et al., 2019). For more information of these earthquakes and to track the latest injection-induced earthquakes, the readers are referred to the Human-Induced Earthquake Database (HiQuake: http://inducedearthquakes.org/) (Wilson et al., 2017).

1.1. Roles of fluid and friction on injection-induced seismicity

The role of fluid pressure in controlling various types of faulting has long been acknowledged, including normal faulting (Sibson, 2000), overthrust faulting (Hubbert and Rubey, 1959), and strike-slip faulting (Hardebeck and Hauksson, 1999). An increase of fluid pressure reduces the effective normal stress and thereby decreases the shear resistance of a fault. The fault can possibly be promoted to slip, which results in natural earthquakes given a sufficiently high fluid pressure. Similarly, injection-induced earthquakes are primarily attributed to the fault reactivation directly or indirectly caused by the fluid pressure increase associated with fluid injection. We schematically illustrate in Fig. 1 how the fluid pressurized zone associated with fluid injection affects the stability of an adjacent pre-existing fault (kilometer-scale) (adapted from (Eaton and Igonin, 2018; Elsworth et al., 2016)). As shown by the changes in the frictional strength and driving shear stress, fluid injection may lower the frictional strength of the fault by reducing the friction coefficient and effective normal stress within the fluid pressurized zone, and could elevate the driving shear stress by transferring stress to the unpressurized zone (e.g., Ellsworth, 2013; Elsworth et al., 2016). The friction coefficient can decrease due to the lubrication effect (e.g., Byerlee, 1967; Cornelio et al., 2019; Diao and Espinosa-Marzal, 2018, 2019; Dou et al., 2020) and chemical effect (e.g., Burnside et al., 2019; Shang et al., 2020), and the reduction in effective normal stress is

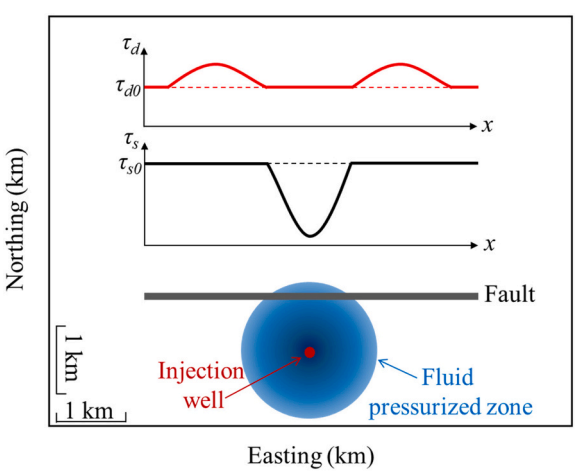

Fig. 1. Schematic map view of injection-induced fault reactivation in the field scale (adapted from Elsworth et al. (2016) and Eaton and Igonin (2018)). The fluid pressurized zone due to fluid injection is drawn assuming the isotropic permeability. x denotes the distance along the fault length. The frictional strength (τ_s) of the fault in the pressurized zone reduces due to the reduction in effective normal stress and/or reduction in friction coefficient, while it keeps relatively unchanged in the unpressurized zone. The driving shear stress (τ_d) along the fault adjacent to the pressurized zone is elevated, while it remains almost constant in the pressurized zone. τ_{s0} and τ_{d0} are the initial frictional strength and driving shear stress, respectively.

associated with fluid pressure buildup and diffusion (e.g., Cappa et al., 2018; Ji et al., 2020). The injected fluid can also drive in-situ fluid into remote faults due to the induced pressure gradient (Brown and Ge, 2018). The diffusion of fluid pressure is sensitive to fluid injection and diffusion rates (Ji et al., 2020), which thus can also be affected by different injection protocols (Ji et al., 2021b, 2021d). If the fluid pressure distributes heterogeneously on faults, the fluid pressure at fault failure can be underestimated by the Mohr-Coulomb failure criterion incorporating Terzaghi's effective stress (Ji et al., 2020; Passelègue et al., 2018; Rutter and Hackston, 2017). Furthermore, the injection of cold water into hot reservoirs can induce tensile stresses in the wall rock of faults by thermal shock (e.g., Zhou et al., 2018). These findings highlight the importance of hydraulic properties of faults as well as the physical and chemical properties of injected fluid in controlling injection-induced seismicity.

Injection-induced fault slip may also be heterogeneous due to the spatial variation of frictional properties (Bhattacharya and Viesca, 2019; Cappa et al., 2018; Guglielmi et al., 2015). This could be further complicated by fluid pressurization, which can alter the velocity-dependency of fault friction, possibly changing the seismic response of faults (Cornelio and Violay, 2020a; Scuderi and Collettini, 2016; Xing et al., 2019). A marked similarity has been reported in several field cases that aseismic slip is first induced by localized fluid pressurization on the velocity-strengthening fault segment, and subsequently, seismic slip is triggered in the unpressurized fault segment characterized by velocity-weakening property due to the enhanced shear stress. Typical field examples include the mine scale experiment injecting fluid into a fault cutting through a carbonate formation in France (Guglielmi et al., 2015), the 2016 M_w 4.1 earthquake resulting from hydraulic fracturing in Duvernay shale, Western Canada (Bao and Eaton, 2016). These observations also cast doubt on the common assumption that injection-induced earthquakes are confined within the stimulated reservoir volume (McGarr, 2014; McGarr and Barbour, 2018), which may further invalidate the established relationships between the maximum magnitude of injection-induced earthquakes and the stimulated reservoir volume (Shapiro et al., 2011), or the injected volume (McGarr, 2014). Thus, the intrinsic and/or injection-altered frictional characteristics of faults strongly affect the occurrence and magnitude of injection-induced earthquake.

1.2. Development of fault friction law

The role of fault stability in controlling earthquakes has been first recognized by Brace and Byerlee (1966), who propose that the laboratory observed stick-slip instability during sliding along laboratory rock fault may be analogous to what happens along tectonic faults during shallow earthquakes. Given the paramount importance of fault behavior in understanding earthquake mechanisms, a vast body of experimental work has been carried out to decipher the mystery of diverse fault behaviors. Particularly, a few pioneering studies have been performed to investigate the factors controlling the properties of rock friction (e.g., Dieterich, 1972, 1978, 1979; Scholz and Engelder, 1976), and the conditions under which the stick-slip instability may occur (e.g., Dieterich, 1979; Ruina, 1983). So far, the rate-and-state friction (RSF) law has been well formulated based on these seminal works to describe the rock friction evolution and define the fault stability criterion (detailed in Section 2) (Marone, 1998; Scholz, 1998). Although RSF law is generalized purely empirically based on laboratory data, it has been successfully employed to reproduce the full spectrum of earthquake failure modes spanning from stable slip, slow slip to unstable stick-slip (e.g., Leeman et al., 2016, 2018; Scuderi et al., 2016; Tinti et al., 2016). Some attempts have also been made to offer microphysical explanations for RSF law (e.g., Chen et al., 2017; Ikari et al., 2016). It is well acknowledged that RSF law can satisfyingly describe rock friction at low slip velocity, while at high slip velocity during co-seismic slip, fault weakening induced by transient frictional thermal effect (e.g., thermal

pressurization of pore fluid and flash heating of highly stressed micro-asperities) could be a supplementary mechanism responsible for the dynamic earthquake rupture (e.g., Acosta et al., 2018; Di Toro et al., 2006; Rice, 2006; Wibberley, 2002; Wibberley and Shimamoto, 2003, 2005).

1.3. Clarification of terminology

Here we clarify the terminology used in this review. The two terms, "fault" and "fracture" are normally used equivalently in most literature, although strictly they may be different in terms of the scale and infill material. In this sense, a large bare fracture in rock masses may evolve to be a gouge-filled fault by developing a finite amount of shear displacement, during which process brecciation is produced progressively by damaging fracture asperities, and sometimes adjacent rocks (Zoback, 2010). In laboratory experiments, fractures and faults are commonly simulated by sawcut, natural, tensile-induced, or triaxial loading-induced rock fractures (e.g., Byerlee, 1967; Ji and Wu, 2020), and granular powders with various sizes (e.g., Marone and Scholz, 1989) and components (e.g., Tembe et al., 2010). In this review, the jargon "fault" is used as the general term to represent the planar discontinuity having relatively low or zero tensile strength. Correspondingly, "reactivation", as opposed to "activation", is used to describe fault failure because of the substantial preceding shear displacement along the fault. We use "injection-induced" seismicity in this review rather than "injection-triggered" seismicity to maintain consistency with the current convention, but we do notice the differences between these two terms (Dahm et al., 2015). One proposed differentiation is that the seismicity is referred as induced if the fault rupture zone is confined within the fluid pressurized zone, while it is regarded as triggered once the rupture zone nucleates or extends beyond the pressurized zone (Lei et al., 2020). In addition, we distinguish between rupture nucleation and the subsequent slip (Acosta et al., 2019; Passelègue et al., 2020) when describing the whole process occurring during injection-induced seismicity.

1.4. Scope and structure of content

This review is tailored towards the laboratory experiments on fault behavior for better understanding of injection-induced seismicity rather than natural earthquakes. First, we present the basics of fault strength and stability, including the Mohr-Coulomb failure criterion, Amotons' law, as well as RSF law. Then, the paradox of fault stability arising from stability analysis in the framework of friction law is discussed. Second, we describe the laboratory methods from the aspects of sample preparation, fluid pathway and stress path. Several useful auxiliary techniques for assisting the interpretation of laboratory results are also mentioned. Third, we comprehensively review the laboratory results in terms of the effects of six different factors including fault properties, stress state, temperature, fluid physics, fluid chemistry and injection protocol to shed light on the mechanisms of injection-induced seismicity. Last, we summarize the questions that have been answered and highlight the open questions to be addressed by future laboratory studies based on this state-of-the-art review.

2. Basics of fault behavior

2.1. Fault strength and stability

The Mohr-Coulomb failure criterion (Jaeger and Cook, 1979; Labuz and Zang, 2012) has been widely employed to describe the fault strength (Sibson, 1986, 1990; Sibson, 1992), which takes the following form,

$$\tau = c + \mu\sigma'_n = c + \mu(\sigma_n - p) \quad (1)$$

where τ is the shear strength, c is the cohesion, μ is the friction coefficient, σ'_n is the effective normal stress, and σ_n and p are the normal stress and pore pressure on the fault, respectively. Although some studies show that the fault cohesion may not be always zero, especially when clay minerals are presented (Ikari and Kopf, 2011), it is still reasonable to take a zero cohesion for faults due to the extremely low value (Zoback, 2010).

Setting the cohesion term in Eq. (1) to zero, the Mohr-Coulomb failure criterion reduces to the well-known Amontons' law of friction (Hubbert and Rubey, 1959; Lapusta and Barbot, 2012; Scholz, 2019),

$$\tau = \mu\sigma'_n = \mu(\sigma_n - p) \quad (2)$$

As expressed in Eq. (2), Amontons' law of friction asserts a proportionality between the shear stress and effective normal stress on a fault plane, with the coefficient of proportionality being referred as the friction coefficient. Note that the friction coefficient (μ) in Eq. (2) is a material property describing the friction of a pre-existing fault, while the internal friction coefficient (μ_r) of an intact rock is a parameter that quantitatively describes how the strength of intact rock increases with elevating confining pressure. It is also noted that the Amontons' law is not derived from the Mohr-Coulomb failure criterion. However, it is interesting that they share the same form. In most cases, the Mohr-Coulomb failure criterion and the Amontons' law of friction are used interchangeably when talking about rock friction. In this review, the Mohr-Coulomb failure criterion is used hereafter. According to Eq. (2), various changes in stress state, pore pressure and friction coefficient in geo-energy reservoirs can result in fault reactivation.

The frictional response of faults (i.e., stable or unstable) upon reactivation is crucial to the evaluation of the potential seismic hazard in geo-energy systems, because the unstable slip along laboratory rock faults is considered as an analogue of earthquakes (Brace and Byerlee, 1966). In seismology, the displacement-driven frictional response of a fault can be described by RSF law as (Fig. 2) (Dieterich, 1979; Marone, 1998; Ruina, 1983; Scholz, 1998, 2019),

$$\mu = \mu_0 + aln\left(\frac{V}{V_0}\right) + bln\left(\frac{V_0\theta}{D_c}\right) \quad (3)$$

where μ_0 is the friction coefficient at steady state when the slip velocity is V_0; $aln(V/V_0)$ is the direct velocity effect; $bln(V_0\theta/D_c)$ characterizes the evolution of μ following an abrupt increase in slip velocity from V_0 to V; a and b are the corresponding scaling coefficients, respectively; θ is the state variable; D_c is the characteristic distance over which the contact population has been renewed.

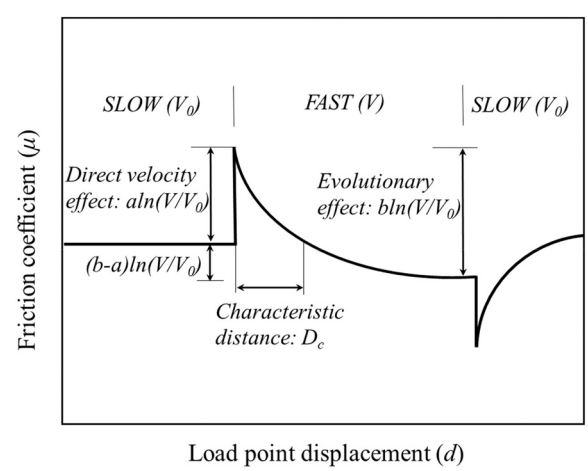

Fig. 2. Schematic diagram showing the frictional response to slip velocity changes, as well as the parameters and terms in the rate-and-state friction law (analytically depicted by Eq. (3)).

If the friction rate parameter (a-b) > 0, μ increases as V increases (i.e., velocity-strengthening), producing only stable slip. In contrast, μ decreases with increasing V (i.e., velocity-weakening) when (a-b) < 0, which accommodates conditionally unstable slip. The sliding on a velocity-weakening fault is unstable when

$$k < k_c = (b-a)(\sigma_n - p)/D_c \tag{4}$$

where k is the stiffness of the elastic surroundings, and k_c is the critical stiffness of the fault (Dieterich, 1979; Marone, 1998; Ruina, 1983; Scholz, 1998). Fault instability occurs due to force imbalance and acceleration when $k < k_c$, because the rate of elastic unloading k is outpaced by the fault weakening rate k_c. Otherwise, the sliding will be stable for a system with higher stiffness, i.e., $k > k_c$. The transition from stable slip to unstable slip involves a stability boundary (i.e., k approximately equal to k_c), where the fault shows quasi-dynamic instability in the form of slow slip with negligible stress drop (Leeman et al., 2016, 2018; Scuderi et al., 2016; Tinti et al., 2016).

2.2. The paradox of fault stability

The most straightforward process underpinning injection-induced fault slip is the increase in pore pressure. After being reactivated, the fault can either slip seismically (i.e., unstable slip) or aseismically (i.e., stable slip) depending on the frictional response. Therefore, the frictional stability in response to fluid injection of a critically stressed fault is used to assess the injection-induced seismic hazard in geo-energy systems. Nevertheless, in the context of RSF law, we may reach paradoxical assertions on injection-induced fault stability. On the one hand, laboratory studies show opposite velocity-dependency of fault friction on pore pressure. In particular, Xing et al. (2019) find that higher pore pressure increases the friction rate parameter (a-b) and thus stabilizes the fault slip. In contrast, Scuderi and Collettini (2016) show that the increase in pore pressure promotes the reduction in friction rate parameter (a-b) and hence favors unstable slip. On the other hand, when it comes to the stability criterion, the increase in pore pressure associated with fluid injection reduces the critical stiffness of the fault (k_c) according to Eq. (4) (Fig. 3), favoring stable slip instead of unstable slip. Specifically, in the spring-slider model, the stiffness of the spring (k) stands for the combined stiffness of the elastic surroundings and the fault. During fluid injection, the pore pressure is increased over the fault under a constant normal stress (σ_n) and a critical shear stress (τ_c). k_c reduces to k'_c with increasing pore pressure, producing stable slip once k'_c is smaller than k. That is, the stability analysis of faults indicates contradictory results on injection-induced fault slip modes, suggesting our poor understanding on the underlying mechanisms of injection-induced seismicity.

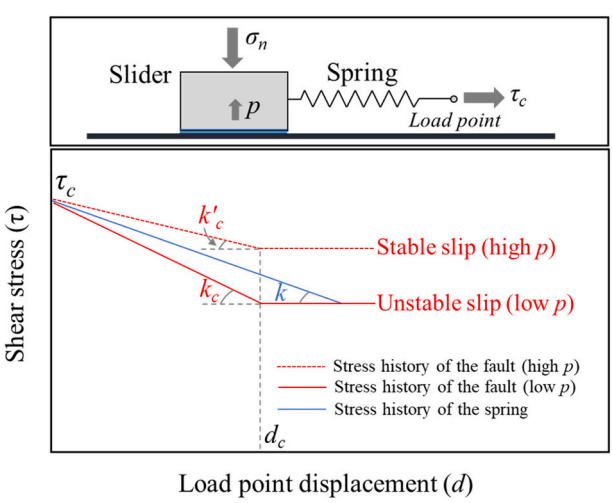

Fig. 3. (Upper) Simplified spring-slider model for stability analysis of a critically stressed fault subject to fluid injection under a constant normal stress (σ_n) and critical shear stress (τ_c). (Lower) The stiffness of the spring (k) stands for the combined stiffness of the testing system and the fault. During fluid injection, the pore pressure (p) in the fault is increased. The critical stiffness of the fault (k_c) reduces with increasing pore pressure (Eq. (4)), promoting stable slip rather than unstable slip when it is smaller than k.

3. Overview of laboratory methods

3.1. Typical experimental setups

Four typical experimental setups have been commonly employed to investigate the fault behavior in the laboratory, including the triaxial shear-flow setup (Fig. 4a) (e.g., Ji and Wu, 2020; Passelègue et al., 2018; Wang et al., 2020a, 2020b), the direct shear-flow setup (Fig. 4b) (e.g., Esaki et al., 1999; Fang et al., 2017; Park et al., 2013; Zhang et al., 2019), the double direct shear-flow setup (Fig. 4c) (e.g., Collettini et al., 2014; Ikari et al., 2009), and the rotary shear-flow setup (Fig. 4d) (e.g., Cornelio et al., 2020; Ma et al., 2014; Passelègue et al., 2016a; Yao et al., 2018). The schematic diagrams in Fig. 4 illustrate only the case in which bare faults are tested with rock matrix. It is noted that fault gouges can also be tested with metal forcing blocks or rock matrix, and fluid can also be introduced into the fault plane using virous methods in the four setups. In addition, it is worth mentioning here that the biaxial shear setup containing an inclined fault plane has also been used frequently (e.g., Buijze et al., 2021; Xia et al., 2004, 2005), but it is not shown in Fig. 4 since it is similar to the triaxial shear setup in terms of the stress state, in which the applied confining and axial stresses can be resolved as the shear and normal stresses on the inclined fault.

3.2. Triaxial shear-flow setup

Compared to the triaxial shear-flow setup, other setups are straightforward regarding the sample preparation, fluid pathway and stress state. Therefore, we detail these three aspects only based on the triaxial shear-flow setup here. The triaxial shear-flow tests can be conducted on an inclined fault in a cylindrical sample and by introducing pore fluid to the fault plane through single or multiple boreholes (e.g., Ji and Wu, 2020; Marone and Scholz, 1989) or porous rocks (e.g., Noël et al., 2019; Wang et al., 2020a, 2020b). The angle of fault plane with respect to the horizontal plane is typically 45° or 60°, which facilitates fault slip without fracturing the rock matrix. The forcing blocks are normally hardened steels and hard rocks when testing gouge materials (e.g., Kohli and Zoback, 2013; Marone and Scholz, 1989) and bare faults (e.g., Ji and Wu, 2020; Ye and Ghassemi, 2018), respectively.

We describe the stress path in the context of Mohr-Coulomb failure criterion in the triaxial shear-flow setup. There are typically two types of shear tests, i.e., displacement-driven, and injection-driven shear tests. In the displacement-driven shear test, either the confining pressure or the normal stress on the fault can be maintained constant (Fig. 5). For the displacement-driven shear test under a constant confining pressure (σ_3) (Fig. 5a), the normal stress (σ_n) and shear stress (τ) on the fault keep increasing with the increase in axial stress (σ_1), according to,

$$\sigma_n = \frac{1}{2}[(\sigma_1+\sigma_3)-(\sigma_1-\sigma_3)cos2\beta] = \sigma_3 + (\sigma_1-\sigma_3)sin^2\beta \tag{5}$$

$$\tau = \frac{1}{2}(\sigma_1-\sigma_3)sin2\beta = (\sigma_1-\sigma_3)sin\beta cos\beta \tag{6}$$

where β is the inclination angle of the fault plane with respect to the horizontal plane. For the fault loading path shown in Fig. 5a, the increases in normal and shear stresses will stop after the steady-state frictional strength is reached.

In many displacement-driven shear tests conducted using the triaxial

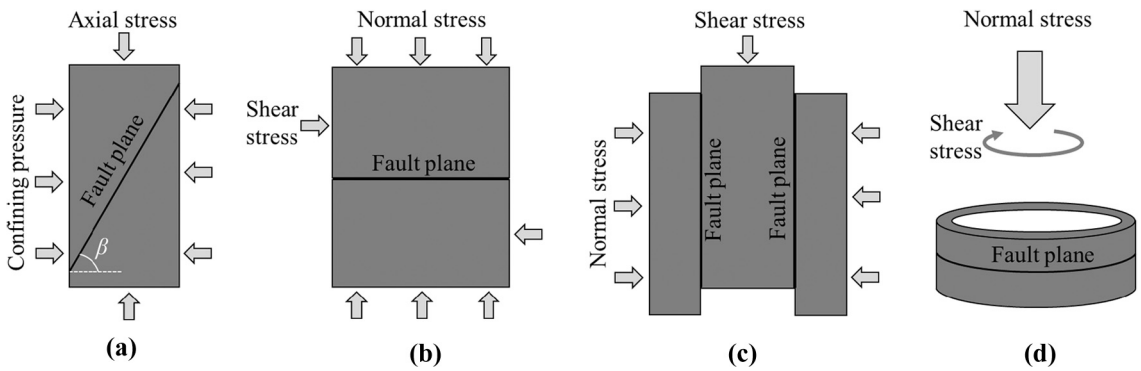

Fig. 4. Experimental setup and stess boundary conditions for shear-flow tests on pre-existing faults. (a) Triaxial shear-flow setup, (b) Direct shear-flow setup, (c) Double direct shear-flow setup, (d) Rotary shear-flow setup. Fluid can be introduced into the fault plane by different methods, which are not shown in this figure.

shear-flow setup, researchers successfully manage to maintain a constant normal stress on the fault by high-speed servo-controlling of the confining pressure to better simulate the fault loading path as applied in the direct shear-flow, double direct shear-flow, and rotary shear-flow setups (Fig. 5b). The contributions of jacket deformation and contact area reduction are also considered on-the-fly to control the stress state on the fault more precisely. The fault slip in the triaxial shear-flow setup is accompanied by the relative horizontal movement of the two sample halves, and thus there is also some discussion on the effects of friction of sample end sliding (e.g., Tembe et al., 2010) or bending moment induced in the axial column associated with the constrained sample ends (Hackston and Rutter, 2016; Mackwell and Paterson, 2002). For the measurement of friction rate parameter (*a*-*b*) in RSF law through velocity-stepping tests using the triaxial shear-flow setup (e.g., Tembe et al., 2010), it is normally performed under the constant normal stress condition (i.e., fault loading path in Fig. 5b) because the rate-and-state effects on fault friction are as small as 1–10% of the frictional strength (Lapusta and Barbot, 2012). It is also worth mentioning that the dilation/compaction of the fault in the normal direction, as a critical parameter, is difficult to measure in the triaxial shear-flow setup. Ye and Ghassemi (2018) have successfully estimated the normal dilation of faults by measuring the shortening and lateral deformation of the sample. However, the measurement of fault dilation/compaction can be easily implemented by using linear variable differential transformers (LVDT) in the other three setups (e.g., Collettini et al., 2014; Scuderi et al., 2017). In addition to the displacement-driven shear tests, force-driven shear tests are also reported (Cornelio et al., 2020), in which the normal stress and pore pressure are kept constant, and the fault slip is induced by manually increasing the shear stress. This also follows the fault loading path shown in Fig. 5b.

3.3. Injection-driven shear tests

In recent years, a growing number of injection-driven shear tests has been performed, which simulates the injection-induced fault slip more realistically because the fault slip is caused by elevating pore pressure on a critically stressed fault. The fault is first loaded to a critical stress state under either a constant confining pressure (Fig. 5a) or a constant normal stress (Fig. 5b). By maintaining a constant shear stress (e.g., Ji, 2020; Scuderi et al., 2017) or a constant displacement (e.g., Passelègue et al., 2018; Wang et al., 2020a, 2020b; Ye and Ghassemi, 2018) condition, the subsequent injection-driven shear test can be conducted under an always fully drained condition, or a locally undrained condition. The major difference between the constant shear stress and constant displacement conditions is that the constant displacement condition can simulate the stress relaxation accompanying fault slip (Passelègue et al., 2018). In this review, we do not intend to differentiate between these two boundary conditions. When the rock matrix is highly permeable, the whole rock sample is always fully drained during the test (e.g., Wang et al., 2020a, 2020b), and the Mohr circle moves towards the failure envelope until fault failure occurs (Fig. 6a). In this case, the Mohr-Coulomb failure criterion is applicable to predicting the fluid pressure at failure. However, the rock matrix can be of extremely low permeability (almost impermeable) and fluid is introduced locally to the fault through drilled boreholes at sample ends (Fig. 6b). The fluid pressure can be homogeneous on the fault under a low normal stress and a slow rate of fluid injection, leading to a fully drained condition, while a high normal stress and a fast rate of fluid injection can cause nonuniform fluid pressure distribution on the fault, resulting in a locally undrained condition (Ji et al., 2020; Passelègue et al., 2018). Here we do not distinguish between the pressure-controlled and volume-controlled fluid injection cases, although these two injection modes can be fairly different especially in the hydraulic fracturing setting presumably due to the significant fluid diffusion in newly created faults or fractures (Zhuang et al., 2019, 2020). However, in our review focusing only on hydraulic shearing, the fast rate of fluid injection collectively refers to either the high volumetric flow rate or fast pressurization rate. In the case of nearly impermeable rock matrix, only the point representing the stress state of the fault moves leftward to approach the failure envelope, rather than the whole Mohr circle. The Mohr-Coulomb failure criterion still applies in the fully drained case with nearly impermeable rock matrix, while it underestimates the fluid pressure at failure in the locally undrained case. Note that, the Mohr-Coulomb failure criterion may always hold in the local scale with a reasonable degree of approximation (Passelègue et al., 2018; Rutter and Hackston, 2017).

The mechanisms leading to the reactivation of a critically stressed fault are different under fully drained and locally undrained conditions (Fig. 7). In the fully drained case, the entire fault is uniformly pressurized by the injected fluid, and the effective normal stress is also reduced near homogeneously (Fig. 7a). The fault reactivation occurs when the driving shear stress exceeds the frictional strength of the fault. The fault rupture front always lags behind the fluid pressurized front (Wang et al., 2020a), which is consistent with the concept of induced and arrested rupture. Under locally undrained condition, the locally introduced fluid accumulates around the injection point and diffuses outwards, causing a significant reduction in frictional strength near the injection point, while that of the remote area remains almost unchanged (Fig. 7b). The reactivation of fault patches beyond the fluid pressure front is driven by the elevation in driving shear stress caused by localized fluid injection (i.e., shear stress transfer) (Elsworth et al., 2016). In this case, the rupture front can exceed the pressure front and reach the unpressurized area (Cebry and McLaskey, 2021; Ji et al., 2021c), which is termed as the triggered and runaway rupture. The competition between the propagation of fluid pressure front and fault rupture front is of great interest and can help understand the processes leading to arrested and runaway ruptures.

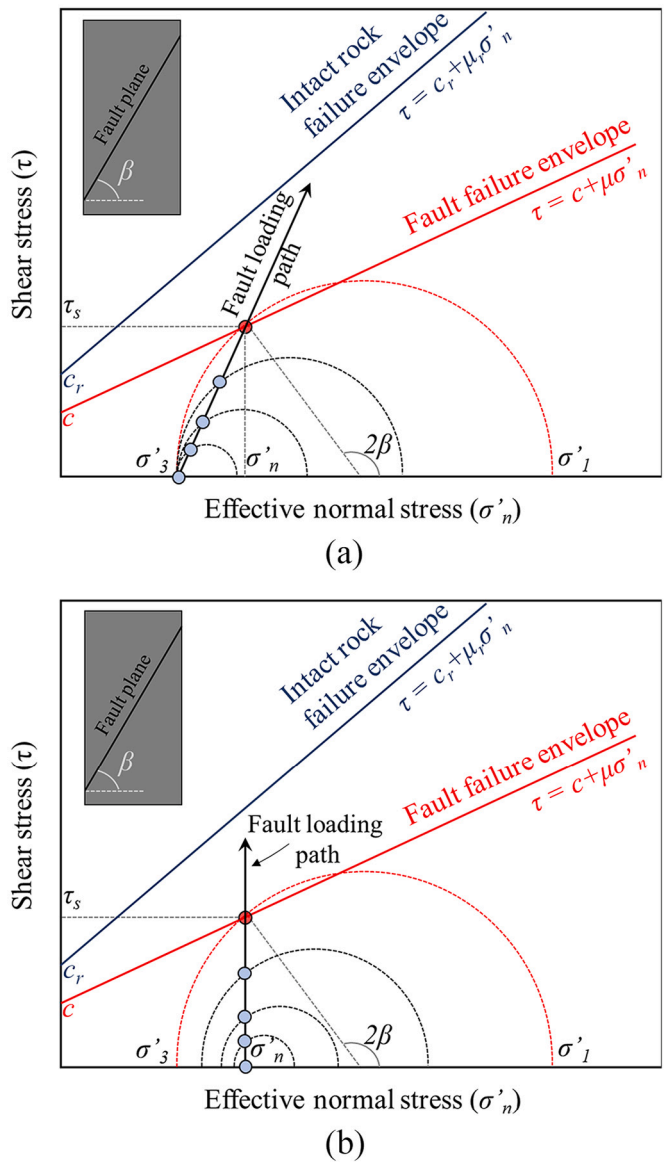

Fig. 5. Stress path in displacement-driven shear test using triaxial shear-flow setup under (a) a constant confining pressure, and (b) a constant normal stress. The normal stress on the fault in (a) is increasing with the increase in axial stress, while the confining pressure in (b) is decreasing with the increase in axial stress to maintain a constant normal stress on the fault. σ'_1 and σ'_3 are the maximum and minimum effective principal stresses, respectively. σ'_n is the effective normal stress. c_r and c are the cohesion of rock matrix and the fault, respectively. μ_r and μ are the internal friction coefficient of rock matrix and friction coefficient of the fault, respectively. τ_s is the shear strength of the fault. β is the angle between the fault plane and horizontal plane.

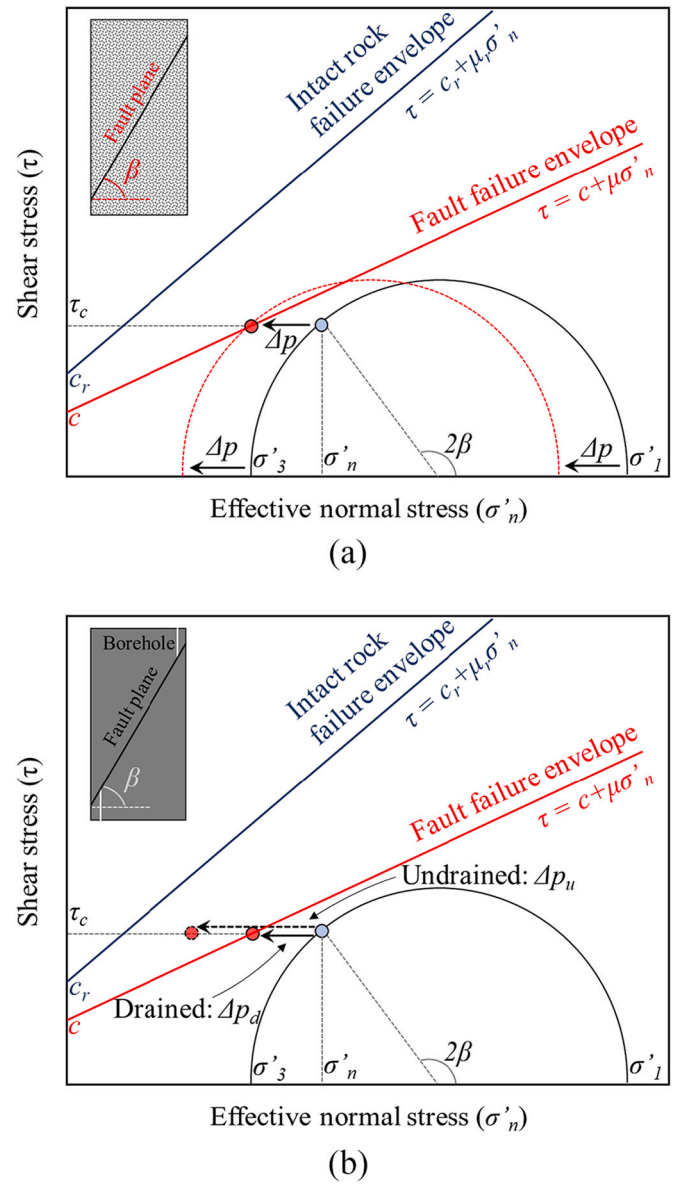

Fig. 6. Stress path in injection-driven shear test on a critically stressed fault under (a) always fully drained condition with highly permeable rock matrix, and (b) locally undrained condition with nearly impermeable rock matrix. Note that the fault can also be drained in (b) if the fluid injection rate and diffusion rate along the fault are balanced. σ'_1 and σ'_3 are the maximum and minimum effective principal stresses, respectively. σ'_n is the effective normal stress. c_r and c are the cohesion of rock matrix and the fault, respectively. μ_r and μ are the internal friction coefficient of rock matrix and friction coefficient of the fault, respectively. τ_c is the critically shear stress on the fault. β is the angle between the fault plane and horizontal plane. Δp is the pore pressure increase at fault failure in the fully drained condition with highly permeable rock matrix. Δp_d and Δp_u are the pore pressure increases at fault failure in the drained and undrained conditions with nearly impermeable rock matrix, respectively.

3.4. Auxiliary techniques

Mechanical data from shear-flow tests are not always sufficient to draw solid conclusions. Sometimes, auxiliary techniques are also indispensable. For example, acoustic emission (AE) technique is an important approach to monitoring the asperity damage and released seismic energy, as well as quantifying the fault rupture front during the injection-driven fault slip (Wang et al., 2020a, 2020b). Ultrasonic wave velocity is measured perpendicular to a critically stressed fault subject to fluid injection to estimate the location of fluid pressure front (Passelègue et al., 2018). Some significant findings are also evidenced by micro-observations of the sample after the experiments. Melted structures from scanning electron microscope (SEM) suggest flash heating as a thermal weakening mechanism during displacement-driven fault instability under dry and low fluid pressure conditions (Acosta et al., 2018). The vanished characteristic peaks of biotite and feldspar in X-ray powder diffraction (XRD) analysis indicate partial melting during the displacement-driven fault instability in Westerly granite (Passelègue et al., 2016b). Apart from the above techniques, we also notice the significance of numerical modelling in better interpreting laboratory results. For instance, numerical modelling has been used to obtain the evolution of hydraulic diffusivity (Almakari et al., 2020) and visualize

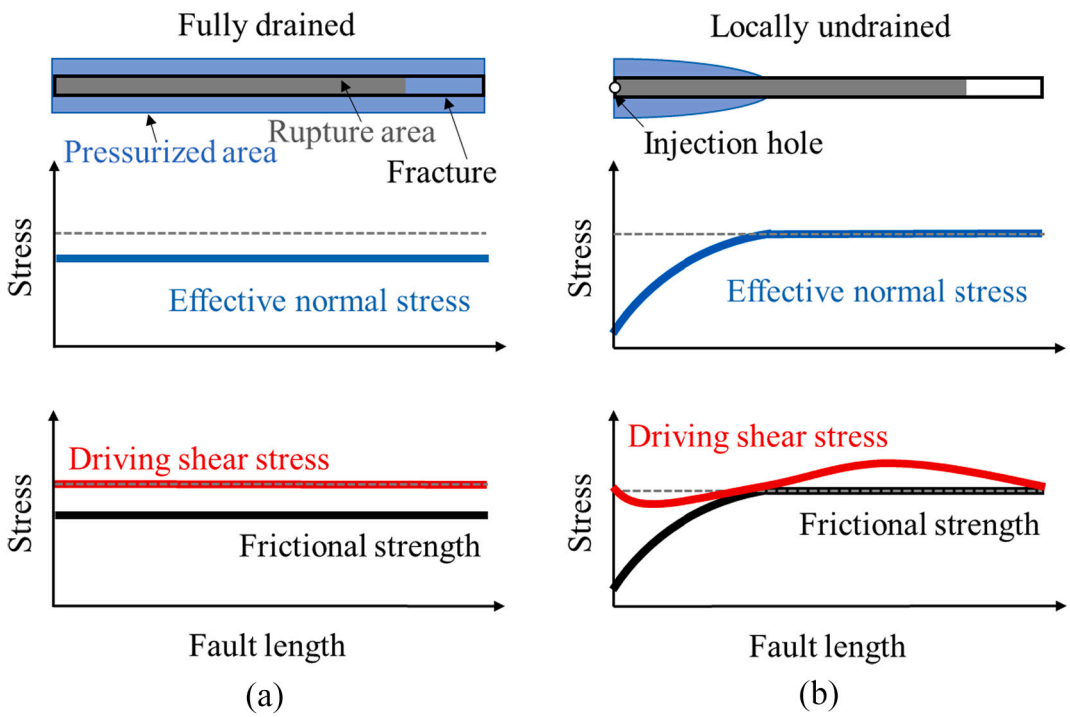

Fig. 7. Schematic diagram showing the evolution of fluid pressurized area (blue shaded area), fault rupture area (gray shaded area) on a single fault (black box), as well as the stress and strength responses of the fault to fluid injection (modified from Ji et al. (2021a)). The gray dashed lines indicate the initial values. (a) Fully drained condition. (b) Locally undrained condition with a local injection hole. Note that the fluid pressurized area is plotted with a larger width than the fault to visualize the magnitude of fluid pressure. (For interpretation of the references to colour in this figure legend, the reader is referred to the web version of this article.)

the fluid pressure distribution (Ji et al., 2020) on critically stressed faults subject to fluid injection based on the inputs obtained from laboratory experiments. Cornelio et al. (2020) exclude the thermal pressurization and confirm the elasto-hydrodynamic (EHD) lubrication as a fault weakening mechanism using numerical modelling. Ji et al. (2021c) demonstrate that the competition among the fronts of fluid pressure, slip, and shear stress transfer is dependent on the fluid pressure distribution on critically stressed faults.

Tables 1 and 2 provide a chronological summary of typical displacement-driven and injection-driven shear tests with particular emphasis on the experimental setup, rock type, fault type, stress path and major observations. Again, note that the purpose of this review is not to include all the experimental tests on fault behavior. Instead, we purposely select the particular experimental studies that further our understanding of injection-induced seismicity. In addition to the mesoscale shear tests listed in Tables 1 and 2, nanoscale displacement-driven shear tests on an atomically flat calcite plane focusing on the effect of water lubrication and fluid chemistry using atomic force microscope (AFM) (Diao and Espinosa-Marzal, 2018, 2019) are also included and discussed. The detailed review and discussion of these studies are presented in Section 4.

4. Laboratory results and implications

The behavior of in-situ faults subjected to fluid injection is controlled by a combination of parameters, including the fault properties, regional stress state, in-situ hydrologic condition, and reservoir temperature. The injected fluid, which is normally in ambient temperature, is pressurized into the target reservoir through various injection protocols. After fluid injection, the physical status and properties of fluid can change in the underground formation and dictate the physical and chemical interactions between fault and fluid. The hydro-mechanical coupling in the reservoir rocks can induce local stress and permeability changes (e.g., Zhang and Mehrabian, 2020a, 2020b, 2021). The temperature contrast between the injected fluid and reservoir rocks can induce tensile stresses through contraction that is termed as thermal shock (e.g., Zhou et al., 2018). Chemical reactions may also occur among the injected fluid, in-situ fluid, and reservoir rocks (e.g., Burnside et al., 2019; Nouailletas et al., 2017; Shang et al., 2020). Experimentalists always seek to understand such complex and fully coupled processes by reasonably simplifying the factor being tested and isolating other dependent factors under well controllable conditions. Here, we summarize six intrinsic, extrinsic, and coupled factors, including fault properties, stress state, temperature, fluid physics, fluid chemistry and injection protocol, which substantially influence the injection-induced fault stability and seismic behavior (Fig. 8). In this section, we critically review the effects of these factors considering the coupling among various factors when necessary.

4.1. *Effect of fault properties*

Fault zones in nature are highly complex with various lithological components and structures, which have a controlling influence on the stability of upper crust (Faulkner et al., 2010). The effects of fault properties on the hydro-mechanical behavior of faults have been extensively investigated and documented. Fault roughness and mineralogy have been shown as the two primary controls.

In the pioneering work on rock friction by Dieterich (1972), smooth faults experience the transition from stable slip to stick-slip behavior under a higher normal stress compared to rough faults. The effect of roughness on the displacement-driven fault slip behavior is further identified and discussed by Dieterich (1978, 1979). These works point out that the fault stability is a system response determined by the contact area of fault surfaces and their elastic surroundings (i.e., testing machine in the laboratory). Specifically, as discussed in Section 2, stable slip only occurs when the rate of elastic unloading of the testing machine is larger than the fault weakening rate, otherwise, faults can exhibit unstable slip. Several attempts have been made to reveal the mechanisms of roughness control on the unstable fault slip. Using focal mechanism heterogeneity monitored by an advanced AE technique as a proxy for microscale stress

Table 1
Summary of typical laboratory studies on displacement-driven shear test on faults.

Experimental setup	Rock type	Fault type	Stress path	Major observation	Reference
a) Without fluid (dry)					
Triaxial shear setup	Westerly granite	Triaxial loading-induced and sawcut faults	5a	Effects of fault roughness on fault instability	Brace and Byerlee (1966)
Double direct shear setup	Sandstone quartzite, graywacke and granite	Sawcut fault	5b	Effects of rock type on the time-dependent rock friction	Dieterich (1972)
Double direct shear setup	Westerly granite	Sawcut fault	5b	Effect of normal stress on friction rate parameter	Kilgore et al. (1993)
Rotary shear setup	Westerly granite	Bare sawcut fault and granite gouge	5b	Effect of large displacement on friction rate parameter	Beeler et al. (1996)
Rotary shear setup	Westerly granite	Sawcut fault	5b	Effects of shear displacement, slip rate and shear heating on friction rate parameter	Blanpied et al. (1998)
Rotary shear setup	Tonalite from the host rock of the Gole Larghe fault zone	Sawcut fault	5b	Effect of melt lubrication on fault weakening	Di Toro et al. (2006)
Triaxial shear setup	NA	Shale gouge	5b	Effects of mineral components on frictional strength and friction rate parameter	Kohli and Zoback (2013)
Double direct shear setup	NA	Quartz gouge	5b	Effects of loading system stiffness on fault slip modes and associated elastic properties of fault	Tinti et al. (2016)
Double direct shear setup	Westerly granite	Sawcut fault	5b	Effect of normal stress change on fault friction	Kilgore et al. (2017)
Triaxial shear setup	Fontainebleau sandstone	Sawcut fault	5a	Effect of fault orientation on fault behavior	Hayward and Cox (2017)
Triaxial shear setup	Westerly granite	Sawcut fault	5a	Effect of frictional heating on fault weakening	Aubry et al. (2018)
Triaxial shear setup	Pietraserena sandstone	Clay-rich gouge	5a	Effect of gouge thickness on stress rotation and fault strength	Giorgetti et al. (2019)
Rotary shear setup	Zhaoyuan Gray granite	Sawcut fault	5b	Effect of cyclic normal stress on fault friction	Sheng et al. (2020)
Triaxial shear setup	Westerly granite	Triaxial loading-induced and sawcut faults	5a	Effect of fault roughness on the seismic/aseismic precursors before stick-slip event	Dresen et al. (2020)
Biaxial shear setup	PMMA forcing blocks	Homogeneous gypsum gouge-filled fault; Heterogeneous gouge fault composed of calcite/quartz/kaolinite	5a	Effect of heterogeneous gouge segments on fault slip behavior	Buijze et al. (2021)
b) With fluid					
Triaxial shear-flow setup	Westerly granite	Triaxial loading-induced, tensile-induced and sawcut faults	5a	Effects of fault roughness and water lubrication on fault friction	Byerlee (1967)
Triaxial shear-flow setup	NA	Quartz gouge	5b	Effect of particle size on shear behavior of fault	Marone and Scholz (1989)
Triaxial shear-flow setup	Westerly granite	Granite gouge	5b	Effects of high temperature and pore pressure on frictional strength and friction rate parameter	Blanpied et al. (1995)
Direct shear-flow setup	Kimmeridge shale	Natural fault in shale	5b	Effect of increasing shear displacement on permeability evolution	Gutierrez et al. (2000)
Double direct shear-flow setup	NA	Three types of clay-rich gouges: chlorite-rich, illite-rich and montmorillonite-rich gouges	5b	Effect of clay minerals on frictional strength, friction rate parameter and permeability evolution	Ikari et al. (2009)
Double direct shear-flow setup	NA	Quartz gouge	5b	Effect of shear-induced dilatancy on fault hardening due to transient pore fluid depressurization	Samuelson et al. (2009)
Direct shear-flow setup	NA	Gouge made from the drill core material from gas field in The Netherland	5b	Effects of brine and supercritical carbon dioxide on frictional strength and friction rate parameter	Samuelson and Spiers (2012)
Triaxial shear-flow setup	NA	Antigorite serpentinite gouge	5a	Effects of increasing shear displacement on permeability anisotropy development	Okazaki et al. (2013)
Double direct shear-flow setup	NA	Soda-lime glass beads	5b	Effect of humidity on fault dynamic instability	Scuderi et al. (2014)
Double direct shear-flow setup	NA	Carbonate gouge	5b	Effect of fluid pressure on friction rate parameter	Scuderi and Collettini (2016)
Direct shear-flow setup	Green river shale and Opalinus shale	Sawcut fault	5b	Effect of mineral on the coupled evolution of frictional stability and permeability	Fang et al. (2017)
Direct shear-flow setup	NA	Smectitic gouge	5b	Effect of transient pore fluid pressure increase in low-permeability fault on the measurement of friction rate parameter and fault weakening	Faulkner et al. (2017)
Triaxial shear-flow setup	Pennant sandstone, Westerly Granite, Bowland shale	Sawcut fault	5b	Effects of normal and shear stresses on permeability	Rutter and Mecklenburgh (2018)
Direct shear-flow setup	Green River shale, Opalinus claystone, Marcellus shale,	Sawcut and sintered faults	5b	Effect of minerals on frictional strength, friction rate parameter and permeability	Fang et al. (2018b)

(*continued on next page*)

Table 1 (*continued*)

Experimental setup	Rock type	Fault type	Stress path	Major observation	Reference
	Tournemire shale, Longmaxi shale and Newberry tuff				
Direct shear-flow setup	NA	Artificial fault with different roughness	5b	Effect of fault roughness on the coupled evolution of frictional stability and permeability	Fang et al. (2018a)
Direct shear-flow setup	Westerly granite	Sawcut fault	5b	Effects of changes in asperity contact distribution and shear-induced dilation on coupled evolution of frictional stability and permeability	Ishibashi et al. (2018b)
Triaxial shear-flow setup	Westerly granite	Sawcut fault	5a	Effect of fluid pressure on fault weakening (flash heating)	Acosta et al. (2018)
Triaxial shear-flow setup	Berea sandstone	Antigorite, olivine, quartz, and chrysotile gouge	5a	Effect of pore pressure on friction rate parameter	Xing et al. (2019)
Triaxial shear-flow setup	Fontainebleau sandstone	Sawcut fault	5a	Effect of cyclic fluid pressurization on fault stability	Noël et al. (2019)
Direct shear-flow setup	Lapeyrate granite	Sawcut fault	5b	Effect of viscosity on slip behavior	Cornelio et al. (2020)
Triaxial shear-flow setup	Westerly granite	Bare sawcut fault and quartz gouge	5a	Effect of transient pore fluid pressure on fault behavior	Proctor et al. (2020)

Table 2
Summary of typical laboratory studies on injection-driven shear test on faults.

Experimental setup	Rock type	Fault type	Stress path	Major observation	Reference
Triaxial shear-flow setup	Medium-grained granodiorite	Sawcut fault	6b	Effect of fault roughness on slip and permeability evolution	Nemoto et al. (2008)
Triaxial shear-flow setup	Pennant sandstone and Darley Dale sandstone	Bare sawcut fault; quartz gouge	6a and 6b	Effect of fluid pressure distribution on the effective normal stress law	Rutter and Hackston (2017)
Triaxial shear-flow setup	Westerly granite	Sawcut fault	6b	Effects of stress state and injection rate on injection-induced fault activation	Passelègue et al., 2018
Double direct shear-flow setup	NA	Carrara marble gouge	6b	Effect of fluid overpressure on fault weakening	Scuderi et al. (2017)
Double direct shear-flow setup	NA	Rochester shale gouge	6b	Effects of fluid pressurization and velocity-strengthening on fault slip	Scuderi and Collettini (2018)
Triaxial shear-flow setup	Sierra White granite	Sawcut and tensile-induced faults	6b	Effect of injection-induced fault slip on permeability evolution	Ye and Ghassemi (2018)
Triaxial shear-flow setup	Inada medium-grained granite	Tensile-induced faults	6b	Effect of injection-induced fault slip on permeability and seismicity	Ishibashi et al. (2018a)
Triaxial shear-flow setup	Bentheim sandstone	Sawcut fault	6a	Effect of fluid injection rate on fault slip behavior and seismic moment release	Wang et al. (2020a, 2020b)
Triaxial shear-flow setup	Bukit Timah granite	Sawcut fault	6b	Effect of fluid pressure distribution on fault reactivation and fluid pressure at fault failure	Ji et al. (2020)
Triaxial shear-flow setup	Bukit Timah granite	Natural and sawcut faults	6b	Effect of fault roughness on injection-induced fault slip behavior	Ji and Wu (2020)
Direct shear-flow setup	Beishan granite	Sawcut and tensile-induced faults	6b	Effect of water lubrication on fault reactivation	Dou et al. (2020)
Triaxial shear-flow setup	Sierra White granite	Tensile-induced fault	6b	Effect of fault roughness on injection-induced slip heterogeneity	Ye and Ghassemi (2020)
Direct shear-flow setup	Polymethyl methacrylate (PMMA)	Sawcut fault	6b	Effect of fluid pressure distribution on rupture nucleation and propagation	Cebry and McLaskey (2021)
Triaxial shear-flow setup	Gonghe granite	Natural fault	6b	Effect of cyclic injection on fault slip behavior	Ji et al. (2021d)
Triaxial shear-flow setup	Bukit Timah granite	Sawcut fault	6b	Effect of cyclic injection on energy budget of fault reactivation	Ji et al. (2021b)
Triaxial shear-flow setup	Barre granite	Sawcut and tensile-induced faults	6b	Effect of fault temperature on fault slip and permeability evolution	KC and Ghazanfari (2021)

field heterogeneity, Goebel et al. (2017) reveal that the local stress field is more homogeneous on a smooth fault than on a rough fault during stick-slip failure (Fig. 9) and this could be the reason for the larger seismic event on a smooth fault during stick-slip failure. Latterly, Dresen et al. (2020) show that the preparatory processes of stick-slip failure on a smooth fault is more seismic compared to that on a rough fault, also drawing on the AE technique.

The simultaneous evolution of frictional properties and permeability of faults is also significantly dictated by the fault roughness. According to Fang et al. (2018a), rough faults are normally characterized by higher frictional strengths and more positive velocity-strengthening behavior due to the cohesive interlocking effect of larger asperities. A transition from velocity-strengthening, to velocity-neutral and finally to velocity-weakening has been observed during the displacement-driven shear of both rough and smooth faults, which is attributed to the shear-induced asperity damage. However, the permeability of smooth fault decreases monotonically due to shear compaction, while that of the rough fault fluctuates because of the alternation between shear compaction and dilation. Ishibashi et al. (2018) investigate the frictional stability of sawcut faults in Westerly granite under controlled pore pressure and normal stress conditions, and they observe a velocity-weakening behavior accompanied by permeability enhancement. This phenomenon is possibly caused by the changes in asperity contact distribution and shear-induced fault dilation associated with slip velocity changes.

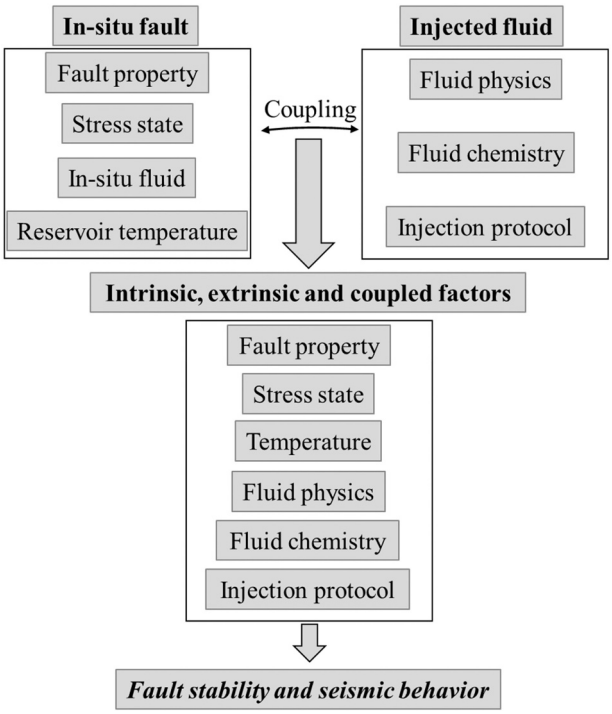

Fig. 8. Diagram showing the interplay among in-situ reservoir conditions and the injected fluid properties. Six intrinsic, extrinsic, and coupled factors are summarized, which control the injection-induced fault stability and seismic behavior.

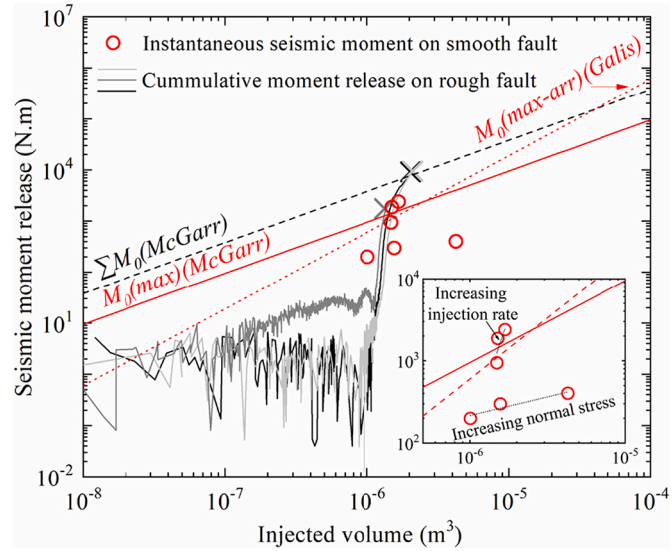

Fig. 10. Seismic moment release on smooth and rough faults in granite as a function of injected volume (replotted with the data in Ji and Wu (2020)). On the rough fault, the cumulative moment release increases progressively with injected volume, and the model proposed by McGarr (2014) holds for the experimentally measured data. The turning points coincide with the onset of fault reactivation. As opposed to the rough fault, the seismic moment on the smooth fault is released abruptly at fault reactivation, and most of points are below the two models proposed by McGarr (2014) and Galis et al. (2017). The inset shows that on the smooth fault, seismic moment increases with increasing normal stress and injection rate. The two outliers are conducted with much higher injection rates.

Injection-induced fault slip is complicated by the various modes of coupled evolution of friction and permeability of faults. Ji and Wu (2020) report the first-ever laboratory experiments that identify the effect of fault roughness on injection-induced slip behavior of critically stressed faults in granite. Particularly, the rough fault releases the seismic moment progressively through quasi-dynamic sliding while the smooth fault shows a sudden release of seismic moment through dynamic slip characterized by obvious shear stress drops (Fig. 10). The experimental data generally comply with the current models relating seismic moment with injected volume (Galis et al., 2017; McGarr, 2014). The turning points towards much faster increasing rates of seismic moment on the curves of rough faults signify the reactivation of the fault. On the smooth fault, the increasing normal stress and injection rate result in larger seismic moment with two out of the six cases exceeding the current models (inset), which will be discussed in detail in Section 4.2. However, it is reported by Ye and Ghassemi (2018) that for both smooth and rough faults in granite, a self-propping dynamic slip

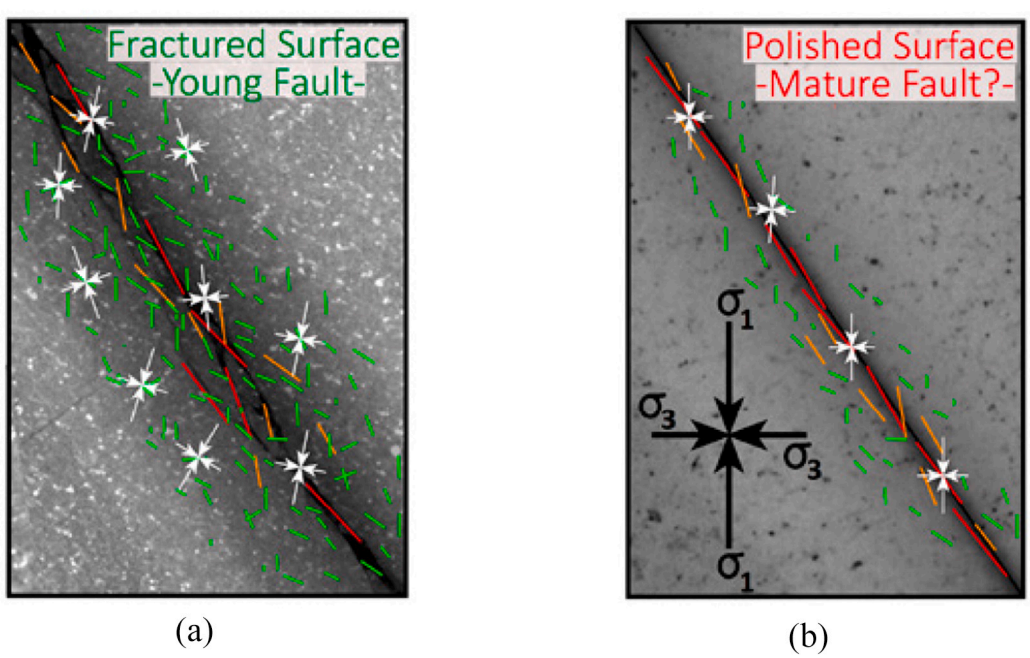

Fig. 9. Schematic diagram illustrating the influence of fault roughness on faulty slip behavior through controlling the distribution of local stress field inferred from AE monitoring (Goebel et al., 2017). Small and large cracks surrounding the fault zone are indicated by green, orange and red lines, respectively. The white and black arrows show the local and macroscopic stress fields, respectively. (a) Heterogeneous local stress field on a rough fault. (b) Homogeneous local stress field on a smooth fault. (For interpretation of the references to colour in this figure legend, the reader is referred to the web version of this article.)

occurs during the stepwise fluid pressurization and the shear-induced permeability enhancement is irrecoverable. This is likely due to the higher normal stress applied in their study, which favors stick-slip failure of faults. In terms of the slip mode and shear dilation, the self-propping dynamic slip reported by Ye and Ghassemi (2018) resembles the stepwise injection-induced slip along faults in granite accomplished by temporal pore pressure drop presented by Nemoto et al. (2008). Besides, Ye and Ghassemi (2020) show with AE hypocenter measurements that the asperity damage can be extremely heterogeneous during the injection-driven slip along a rough fault in granite, similar to the observations in the displacement-driven slip along a rough fault (Dresen et al., 2020).

Apart from fault roughness, the mineral composition of faults is another crucial factor that controls its frictional and hydraulic properties. Because clay minerals are abundant in mature fault zones (e.g., Collettini et al., 2019) and many shale reservoir rocks (e.g., Kohli and Zoback, 2013; Fang et al., 2017), the effect of clay minerals has been the focus of many experimental studies. Kohli and Zoback (2013) carry out a comprehensive study that investigates the effect of clay and organic content on the frictional behavior of shale samples from three hydrocarbon reservoirs (i.e., the Barnett, Haynesville, and Eagle Ford shales in the United States). The transition from velocity-weakening to velocity-strengthening occurs with increasing clay and organic content at ~30 wt%. The evolution of velocity-dependency of fault friction is attributed to the change in the grain-packing framework from rigid clast supported to clay and organic supported. A more recent study also confirms the dependency of grain-packing framework transition on clay and organic matter content using shale samples from Southern Sichuan Basin and the Ordos Basin in China (Wang et al., 2019). Clay minerals can also significantly influence the coupled evolution of frictional stability and permeability. Ikari et al. (2009) investigate the effect of clay types on the friction and permeability evolution with increasing shear displacement on water-saturated clay-rich gouge. The friction coefficient of all the three types of clay-rich gouge is low ($\mu = 0.19$–0.32), and they all show velocity-strengthening behavior. Permeability keeps decreasing with larger shear strain, and permeability reduction is most profound at shear strains smaller than ~5. Montmorillonite and illite gouges show consistently lower permeability than chlorite. The results suggest that clay-rich gouges are intrinsically stable, and the drainage condition of clay-rich gouge depends on both the shear strain and clay type. Fang et al. (2017) study the coupled evolution of frictional stability and permeability of faults in shales with increasing shear displacement under simulated in-situ stress and pore pressure conditions. They find that carbonate-rich shale shows a higher frictional strength, and neutral frictional stability, and its permeability reduction is coupled with the friction evolution, while clay-rich shale is characterized by a lower frictional strength, and strong frictional stability, and its permeability reduction is caused by mineral swelling and thus the permeability evolution decouples with the friction evolution. A more comprehensive study on the mineralogical control of frictional stability and permeability change reveals that frictional strength and permeability change increase with tectosilicate content and reduce with phyllosilicate content (Fang et al., 2018b). Moreover, the friction rate parameter (a-b) is inversely correlated with permeability evolution.

Since the mineral composition has a strong impact on the evolution of frictional and hydraulic properties, the injection-induced frictional response of critically stressed faults is also largely controlled by the mineral composition. Scuderi et al. (2017) demonstrate that velocity-strengthening carbonate gouge, which should favor aseismic creep, can be induced to slip dynamically by fluid pressurization. This happens because the fault strengthening caused by increasing slip velocity is overcome by the fault weakening induced by fluid pressurization. Nevertheless, the illite-rich shale gouge only exhibits a slow injection-induced slip rate upon injection-induced reactivation due to its extremely low permeability normal to the shear plane and strong velocity-strengthening behavior, indicating that the evolving hydraulic properties, and rate-and-state frictional properties collectively control the fault response to fluid injection (Scuderi and Collettini, 2018). Particularly, this evolving hydraulic property refers to the anisotropic evolution of permeability during shearing of fault gouge. A representative study is reported by Okazaki et al. (2013) on antigorite serpentinite gouge. The initial permeabilities of the gouge layer are similar in all directions, while permeability anisotropy develops with increasing shear displacement until the shear stress reaches the steady state, with the permeability normal to the shear plane being lower than the other two orthogonal directions. The anisotropy in permeability evolution is related to the formation of shear localization and can reduce the fluid flow perpendicular to the shear direction. This result suggests that fluid diffusion along a mature fault may have a preferable pathway parallel to the shear direction, which can thus influence the fluid pressure distribution in the fault zone and the potential earthquake nucleation zone. Apart from the permeability anisotropy, a more recent study presented by Kluge et al. (2021) also suggests a nonuniform fault permeability along the shear direction due to the presence of transtensional wedges, simple shear zone, and core compression zones, with the transtensional wedges characterized by the largest permeability. This indicates that fluid buildup and migration could be further complicated by the nonuniform fault permeability, and thereby a complex seismic response.

In summary, the above studies have extensively investigated the effects of roughness and mineralogy of faults on the displacement-driven and injection-driven responses considering macroscopically uniform fault planes. Nevertheless, in-situ faults are always heterogeneous. In light of the spatially heterogeneous fault friction in nature, Buijze et al. (2021) look into the effect of heterogeneous gouge segments simulated by different gouges on the displacement-driven fault slip behavior and find that the displacement-driven fault slip behavior is controlled by gouge friction and stress concentration. The hydraulic properties of frictionally heterogeneous faults can also be heterogeneous, which thus make the injection-induced fault slip much more complex in terms of the permeability evolvement, fluid diffusion and slip mode (Guglielmi et al., 2015). Therefore, future experimental studies considering the injection-induced behavior of a "nonuniform" fault plane is necessary, which is composed of at least two patches each characterized by a particular roughness and/or mineralogy.

4.2. Effect of stress state

The stresses acting on a fault are a result of the prevailing regional stress condition surrounding the fault and strongly dictate the fault behavior. Most studies investigate the influence of the stress state on fault behavior by conducting displacement-driven shear tests. For example, Kilgore et al. (1993) study the velocity-dependent friction of bare Westerly granite surfaces over a wide range of normal stresses (i.e., 5, 15, 30, 70, and 150 MPa), and slip velocities (i.e., 10^{-4}-10^{3} μm/s). At velocities between 10^{-4} and 1 μm/s, consistent velocity weakening behavior is observed, which is more obvious at lower velocities. When the velocity is larger than 10 μm/s, velocity weakening (under 30, 70, and 150 MPa normal stress), velocity neutral (under 15 MPa normal stress), and velocity strengthening (under 5 MPa normal stress) are observed under different normal stresses. These observations suggest that stable slip along faults in granite is favored at shallow depths. This is also in line with the results on granite gouge (Fig. 11), which show a positive friction rate parameter (a-b) at lower normal stresses because of poor consolidation. The friction rate parameter (a-b) reduces with increasing normal stress due to a more consolidated state (Scholz, 1998). In addition to these studies, a vast number of laboratory experiments on lithologies observed or inferred to host induced seismicity (i.e., carbonate, shales, and granite) under depths above ~6–7 km and temperature below <120 °C show that these formations are intrinsically aseismic (Scuderi et al., 2017), which is contrary to the fact that the hypocenters of injection-induced seismic events are in shallow crust. This suggests the need to investigate the effect of stress state through

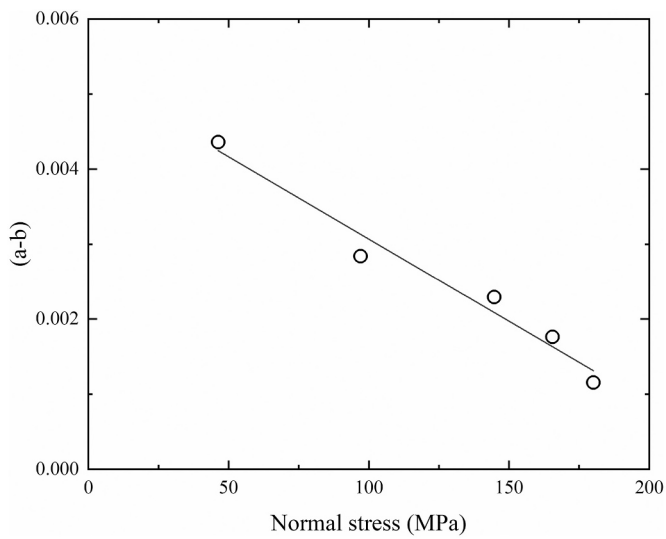

Fig. 11. Friction rate parameter (*a-b*) of granite gouge as a function of normal stress (replotted with the data in Scholz (1998)).

injection-driven shear tests, as reviewed below.

In injection-driven shear tests on critically stressed faults, fluid can either be fully drained or locally undrained on the fault as discussed in Section 3, which is affected by the stress state of the fault. To quantify the fluid pressure heterogeneity on the fault, we define the fluid overpressure ratio as the ratio between the injection pressure at fault failure measured at the injection borehole and the predicted fluid pressure at fault failure from Mohr-Coulomb failure criterion combing with Terzaghi's effective stress law (Ji and Wu, 2020). When the fluid pressure distribution is uniform on the fault, the fluid overpressure ratio is unity, and this ratio increases with more heterogeneous fluid pressure distribution on the fault as demonstrated by Passelègue et al. (2018). Fig. 12 is plotted based on the data extracted from Ji and Wu (2020), Ji et al. (2021a) and Passelègue et al. (2018). It shows that the fluid overpressure ratio increases with higher initial effective normal stress, higher shear stress and faster injection rate. These trends are easy to understand, because the fluid pressure distribution on a fault depends on the balance between fluid injection and diffusion rates. A higher initial effective normal stress squeezes the fault and reduces the fault permeability, making it difficult for the fluid to diffuse along the fault. A higher shear stress means a more critically stressed fault and allows shorter time for the fluid to diffuse. A faster rate of fluid injection promotes the accumulation of fluid around the injection point. Moreover, the

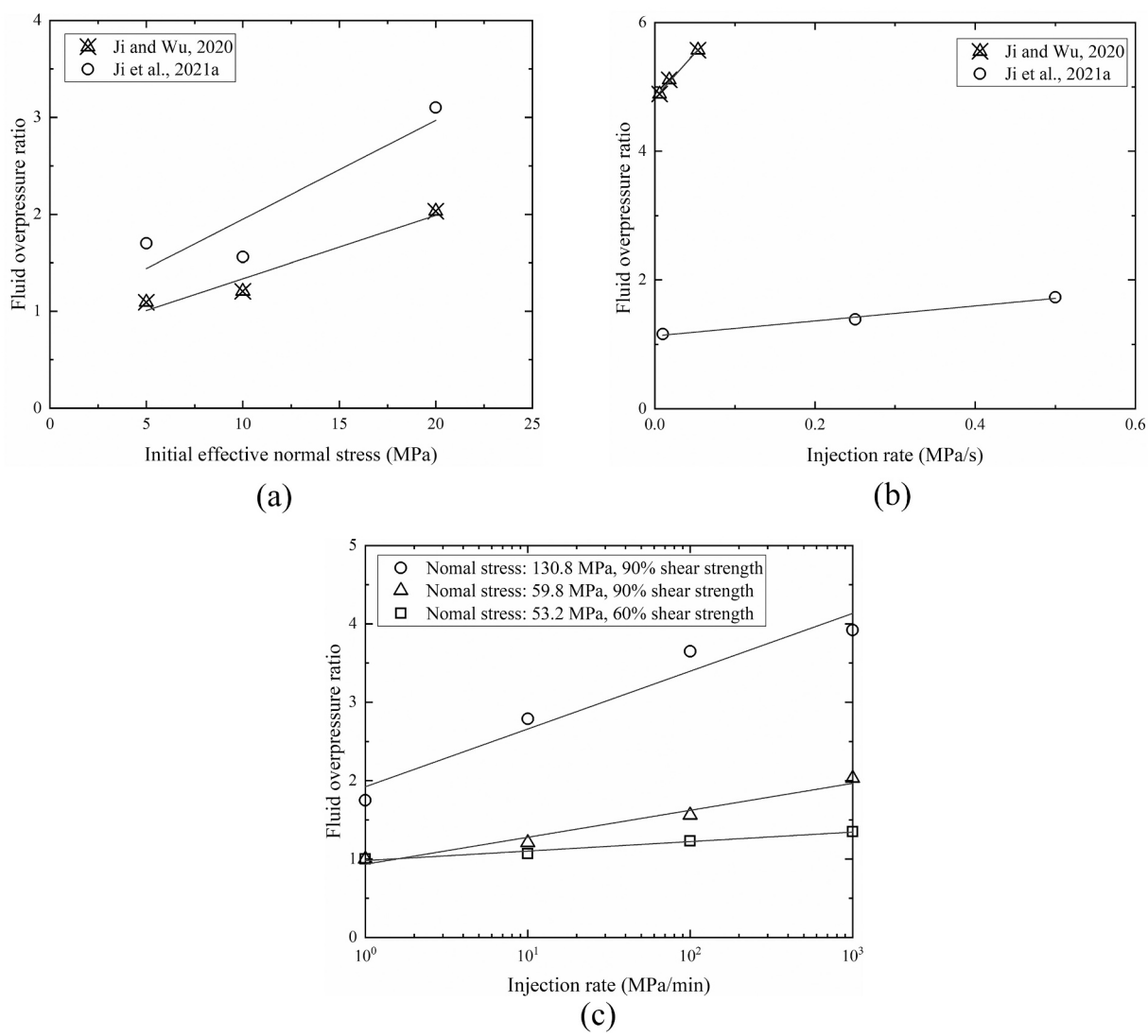

Fig. 12. Fluid overpressure ratio as a function of (a) initial effective normal stress, and (b) and (c) injection rate. (a) and (b) are plotted by compiling the data from Ji and Wu (2020) and Ji et al. (2021a). (c) is plotted with the data extracted from Passelègue et al. (2018).

permeability of tensile-induced faults in granite reduces with increasing shear displacement under higher normal stresses (Shen et al., 2020), indicating that the fluid diffusion along the fault may become increasingly difficult with cumulative shear deformation of the fault when the normal stress is relatively high. The fluid overpressure ratio, determined by the stress state and rate of fluid injection, has been found as a key parameter controlling the injection-induced maximum seismic moment by Ji and Wu (2020). This could be explained by the fact that the localized fluid pressurization acts as a point load to perturb the stability of a critically stressed fault (Garagash and Germanovich, 2012) (Fig. 7). The intensity of the perturbation increases with larger fluid overpressure ratio characterized by a higher fluid pressure at fault failure. As found by Galis et al. (2015), the capability of rupture propagation along a fault scales with the intensity of perturbation. Thus, a larger fluid overpressure ratio at fault failure results in a larger magnitude of seismic moment release from the total elastic energy stored in the sample-testing machine system (Fig. 13a). The slip rate at fault reactivation also increases with larger fluid overpressure ratio as shown in Fig. 13b, which is plotted based on the data extracted from Passelègue et al. (2018). Besides, the total elastic energy stored in the sample-testing machine system (a proxy for the fault-surrounding rock system in the field) also increases with higher initial stress magnitudes, and thus a critically stressed fault can produce a larger maximum seismic moment under higher initial stress magnitudes (i.e., higher normal stress and higher shear stress) (Fig. 14a). This is consistent with the trend shown in Fig. 14b where the rupture velocity increases with initial effective normal stress (Passelègue et al., 2020). Note that there is a difference between rupture propagation during earthquake nucleation and dynamic slip during earthquake instabilities (cf. Acosta et al., 2019). Therefore, we do not compare rupture velocity during slip nucleation with slip velocity at fault reactivation during dynamic slip. Two parameters characterizing the dynamic slip phase, i.e., the maximum seismic moment and slip rate at fault reactivation, both scale with higher fluid overpressure ratio (Fig. 13). Besides, the maximum seismic

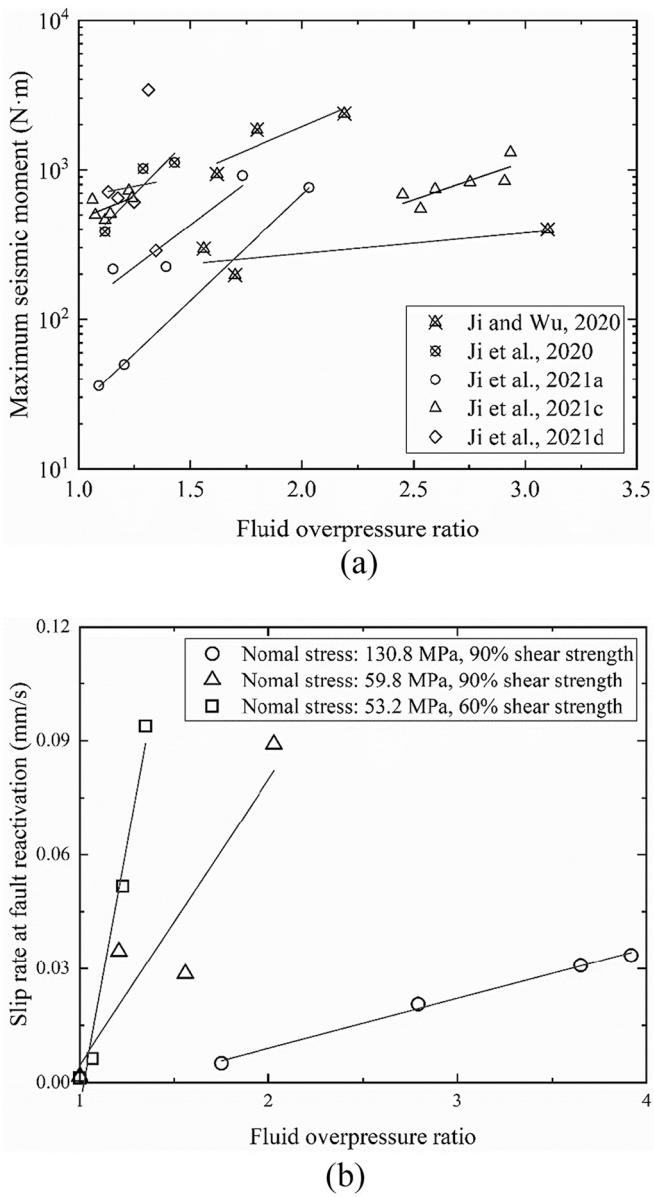

Fig. 13. Effect of fluid overpressure ratio on fault reactivation. (a) Maximum seismic moment and (b) slip rate at fault reactivation as a function of fluid overpressure ratio. (b) is plotted with the data extracted from Passelègue et al. (2018). The straight lines in (a) are the best fit lines for each series of tests on the same sample with changing parameters.

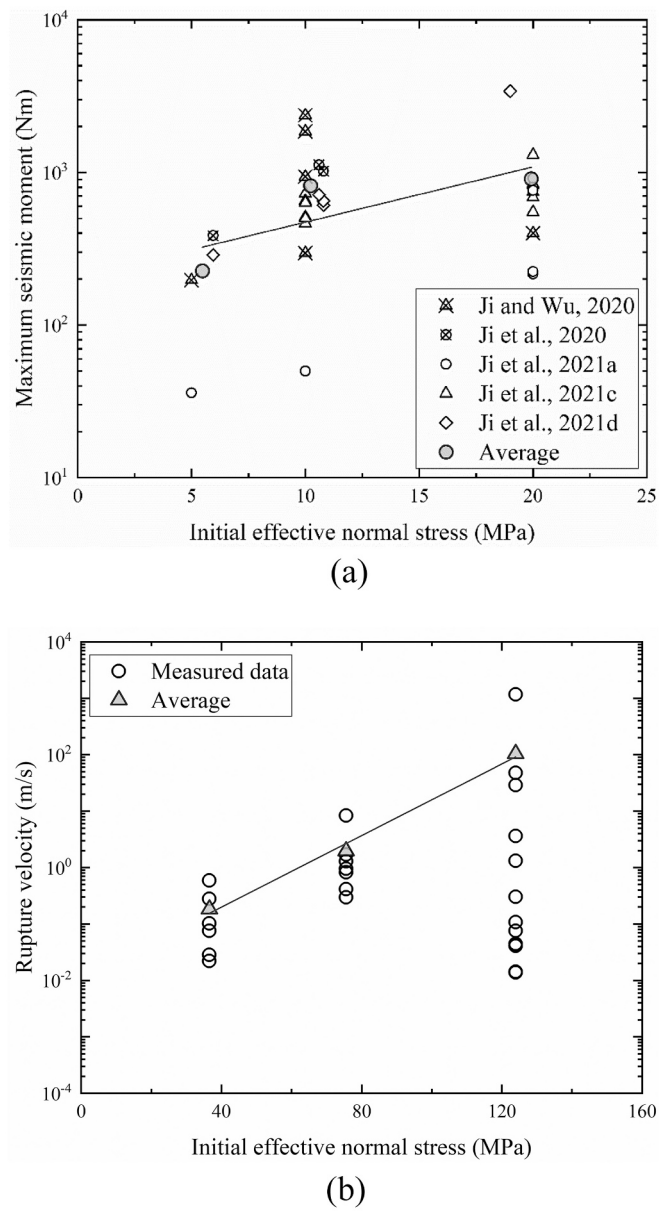

Fig. 14. Effect of initial effective normal stress on fault reactivation. (a) Maximum seismic moment and (b) rupture velocity as a function of initial effective normal stress. (b) is plotted with the data extracted from Passelègue et al. (2020).

moment release during the dynamic slip phase, and the rupture velocity during the slip nucleation phase both increase with higher initial effective normal stress (Fig. 14). A faster rupture velocity during slip nucleation always leads to a faster slip rate at fault reactivation, a larger slip displacement and a larger seismic moment release (Passelègue et al., 2020). Taken together, we may conclude that higher initial stress magnitudes on faults increase the magnitude of injection-induced seismicity. In other words, higher differential stress magnitudes in deep reservoirs containing critically stressed and favorably oriented large faults (Zang and Stephansson, 2009) pose a higher risk of injection-induced seismicity.

The orientation of faults relative to the regional stress state is also important. Most studies as reviewed above have investigated the behavior of faults oriented favorably for slip in the regional stress state. However, faults can be divided into two categories depending on the inclination angle of fault with respect to the prevailing stress state, i.e., favorably, and unfavorably oriented faults. Specifically, according to the Mohr-Coulomb failure criterion, the optimally oriented fault is inclined to the maximum principal stress at 45°-0.5tan$^{-1}\mu_r$, along which the shear stress required for sliding is the minimum. For most rocks, μ_r ranges from 0.5–1.0 and thus the optimal angle is ~25°-30° (Sibson, 1990). Favorably oriented faults refer to faults with inclination angles near the optimal angle, while the angles of unfavorably oriented or misoriented faults are much smaller or greater than the optimal angle. Young faults are always favorably oriented while some can become unfavorably oriented over time. However, most current studies focus on the injection-induced behavior of favorably oriented faults with respect to the applied stress state, which thus only provides the lower limit to fluid overpressure (Lei et al., 2017b). Although favorably oriented faults are the most frequent and susceptible source of seismicity, fluid overpressure still has the potential to activate faults unfavorably oriented for reactivation in the local stress field because of their weakness compared to host rocks. The injection-induced behavior of unfavorably oriented faults can significantly differ from the favorably oriented ones due to physical processes such as melt welding (Fig. 15a, (Hayward and Cox, 2017)) and stress rotation (Fig. 15b, (Giorgetti et al., 2019)). As shown in Fig. 15a, an experimental fault in Fontainebleau sandstone that is unfavorably oriented in the applied stress state can be welded by the micrometer-thick layers generated by frictional melting, which increases the fault cohesion. The subsequent loading of the fault may create new and favorably oriented secondary faults, widening the fault core with episodic slip events. In Fig. 15b, the maximum principal stress tends to rotate to 45° to the fault boundaries within misoriented fault zones with thick gouge layers (e.g., Byerlee and Savage (1992); Lockner and Byerlee (1993), Fig. 15b), enhancing the slip of unfavorably oriented shear zones by reducing the required stress for reactivation. These two mechanisms could complicate the injection-induced behavior of misoriented faults, which remains unclear and necessitates future studies.

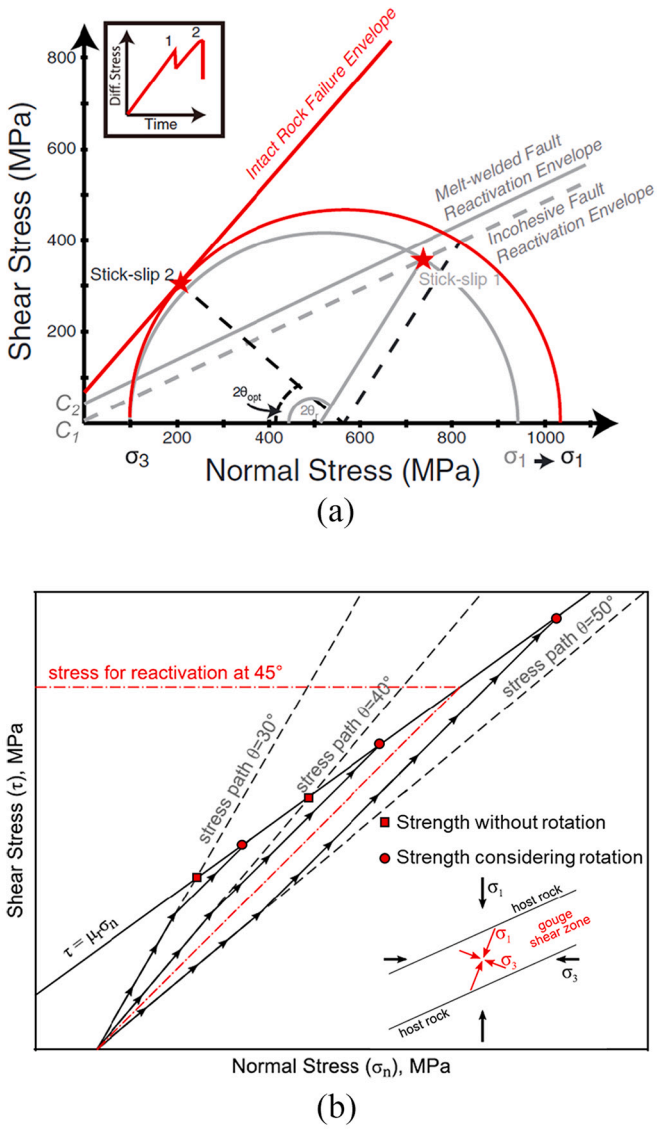

Fig. 15. Effect of unfavorable stress state on fault reactivation. (a) Schematic diagram showing the effect of melt-welding on the behavior of unfavorably oriented fault (modified from Hayward and Cox (2017)). C_1 and C_2 are fault cohesions before and after melt welding. (b) Schematic diagram showing the stress paths of unfavorably oriented faults due to local stress rotation (modified from Giorgetti et al. (2019)). The inset shows schematically how the stress state develops within the gouge layer.

4.3. Effect of temperature

Temperature always plays an important role in controlling the fault behavior in underground formations. For example, a high temperature up to 315 °C can significantly reduce the shear stiffness of sawcut faults in sandstone (Zhang et al., 2019b). In terms of fault stability, Brace and Byerlee (1970) first observe that a high temperature can suppress the occurrence of stick-slip on faults in gabbro and granite. In Section 4.2, we find that higher initial stress magnitudes encourage a faster rupture velocity, resulting in a larger seismic moment (Fig. 14). In this case, there are two opposite trends of injection-induced earthquake likelihood when it comes to the effect of reservoir depth. Particularly, although higher initial stress magnitudes at larger reservoir depth favor larger magnitude injection-induced seismic events (as concluded in 4.2), the brittle-ductile transition of rocks can reach at greater reservoir depth due to the high temperature and elevated stress magnitudes (Paterson and Wong, 2005), tending to inhibit unstable stick-slip. For example, for faults in granite (Fig. 16), the friction rate parameter (*a-b*) can become positive when the temperature is above ~315 °C because of crystal plasticity of quartz (Scholz, 1998), indicating that faults in granite are intrinsically stable in deep geothermal systems with temperature above 315 °C. The question is whether this behavior remains with the presence of pore fluid under elevated temperature. To this end, Blanpied et al. (1995) investigate the frictional behavior of faults in granite containing a layer of granite powder at hydrothermal conditions. The frictional behavior is divided into two regimes. The first regime includes dry granite up to 845 °C and wet granite below 250 °C, and the second regime includes wet granite above 350 °C. The friction coefficient in the first regime (cool and/or dry) is modestly dependent on temperature and slip velocity. While in the second regime (hot and wet), the friction coefficient shows temperature-weakening and velocity-strengthening behavior. The results imply that the fluid-assisted deformation processes on faults in granite are active under high temperature, which

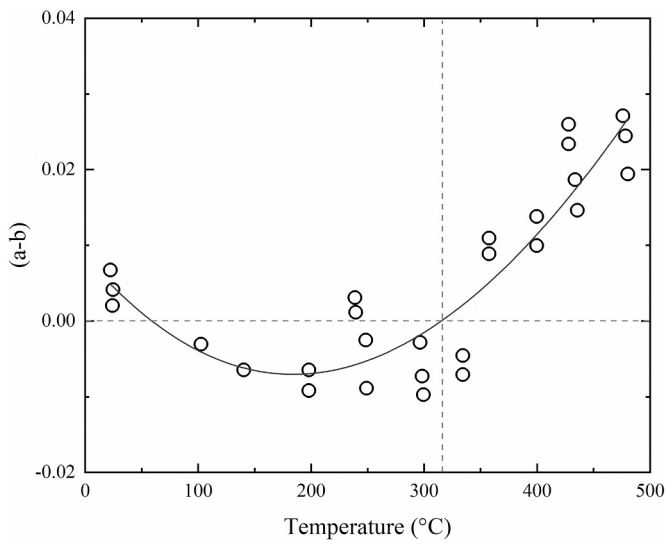

Fig. 16. Friction rate parameter (*a-b*) of bare smooth fault in granite as a function of temperature (replotted with the data in Scholz (1998)).

promote aseismic fault behavior. Lately, an experimental study on colder water injection into a hot pre-stressed fault in granite has been reported by KC and Ghazanfari (2021), and the results show that thermal stress can further damage the asperities in addition to shear crushing while the permeability is enhanced after the shear slip. The gradual decrease of permebaility in the post-hydro-shearing stage may affect the long-term reservoir production primarily due to the clogging of fluid pathway by produced gouge and the closing of fracture by asperity degradation and mineral dissolution under high temperature. However, the interesting question remains enigmatic as to how a critically stressed fault under hydrothermal conditions responds to the injection of pressurized colder water, which allows the direct observation of how hydraulic stimulation can affect the fault behavior in hot dry rocks.

Temperature could also influence fault stability through changing fault permeability. Polak et al. (2003) experimentally study the permeability evolution of a natural fault in Arkansas Novaculite under temperatures ranging from 20 °C to 150 °C, focusing on the influence of mineral dissolution under hydrothermal conditions. They find that the reduction in aperture is mainly caused by the dissolution of stressed apertures in contact. Small temperature change can exert a large impact on aperture change and thus the fault permeability. Yasuhara et al. (2004) simulate this test using a mechanistic model and find that the fault closure rate scales exponentially with temperature due to pressure solution. These results suggest that the stimulated fractures/faults in geothermal reservoirs cannot maintain a high permeability with the elapse of time, which is not good for heat productivity to be maintained and fluid to diffuse through the reservoir. This is backed up by the observation at the geothermal site of Groß Schönebeck, Germany, where the productivity keeps reducing over the course of 2.5 years (Blöcher et al., 2016). In addition, as discussed in Section 4.2, the permeability reduction associated with fault closure tends to favor a larger fluid overpressure ratio, possibly triggering larger magnitude injection-induced seismic events when there are critically stressed faults nearby.

Apart from the background/reservoir temperature, the transient high temperature generated during dynamic slip by frictional heating strongly influences the dynamic fault weakening. There are two main thermal weakening mechanisms during fast fault slip, i.e., thermal pressurization of pore fluid, and flash heating of asperity contacts (Rice, 2006). The transient thermal-induced fluid pressure increase caused by frictional heating may contribute to the weakening of low-permeable faults, while the occurrence of flash heating (normally at ~1000 °C)

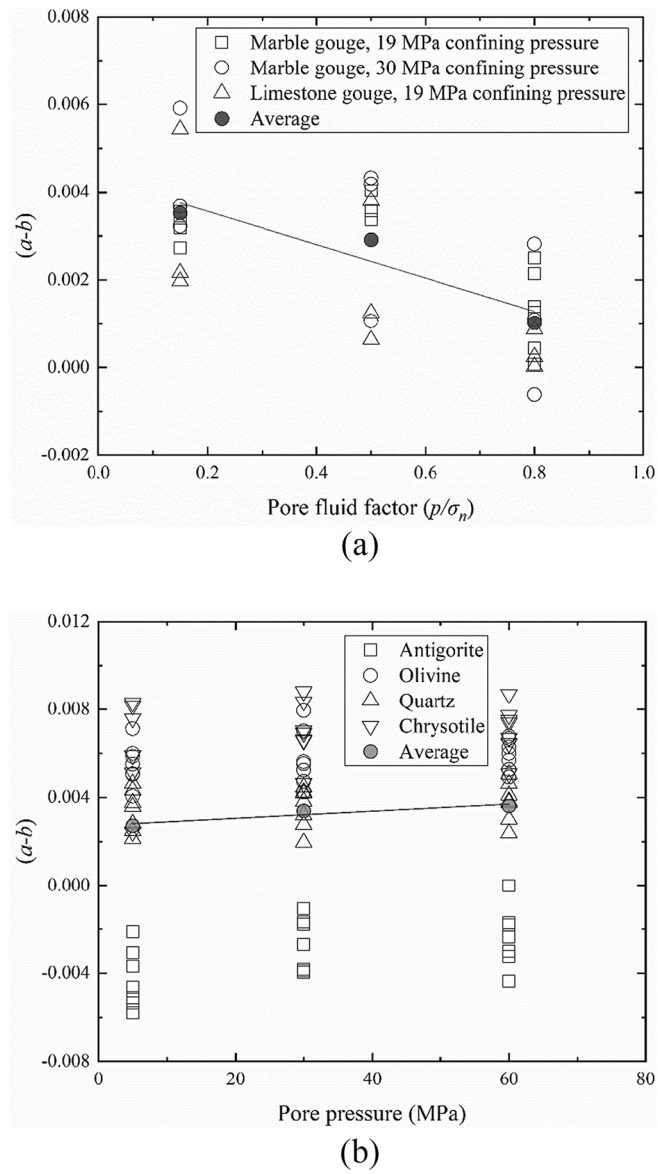

Fig. 17. Effect of pore pressure on friction rate parameter (*a-b*). (a) (*a-b*) as a function of pore fluid factor (p/σ_n) for two gouge materials (plotted with the data extracted from Scuderi and Collettini (2016)). (b) (*a-b*) as a function of pore pressure for four gouge materials (plotted with the data extracted from Xing et al. (2019)).

may require a slip rate as fast as ~10 cm/s in the asperity lifetime (Acosta et al., 2018). This transient high temperature can also cause dehydration of clay minerals, during which the water evaporates and thus reduces the effective normal stress, further contributing to the dynamic fault weakening (Ujiie and Tsutsumi, 2010).

4.4. Effect of fluid physics

Here we use the term fluid physics to refer to the physical state (e.g., pressure and phase) and physical properties (e.g., density, compressibility, viscosity, and thermal diffusivity) of fluid, which is greatly influential in fault behavior. The presence of water can activate water-assisted processes during fault dynamic instability. The stick-slip friction drop and frictional healing rate increase with higher air humidity due to the larger grain-to-grain contact area (Scuderi et al., 2014). The presence of pore pressure may alter the friction rate parameter (*a-b*) of faults. Scuderi and Collettini (2016) study the evolution of RSF

parameters of carbonate gouge with increasing pore pressure from sub-hydrostatic (pore fluid factor $\lambda = 0.15$), to supra-hydrostatic ($\lambda = 0.5$) and to near lithostatic ($\lambda = 0.8$), where the pore fluid factor λ is the ratio between the pore pressure and normal stress. The results show the friction rate parameter (a-b) changes from velocity-strengthening to velocity-neutral (Fig. 17a). They ascribe the decrease in (a-b) to the reduction in layer dilation. In contrary to the results presented by Scuderi and Collettini (2016), Xing et al. (2019) report that the high pore pressure tends to stabilize four type of gouges (i.e., antigorite, olivine, quartz, and chrysotile) signified by the increase in friction rate parameter (a-b) (Fig. 17b). They use the dilatant hardening mechanism to explain the observed change of the friction rate parameter (a-b). The contradictory trends of (a-b) with increasing pore pressure are most likely attributed to the differences in effective stress, porosity, strain rate and mineralogy in these two independent studies. However, the opposite results suggest our poor understanding of pore pressure effect on the friction rate parameter (a-b) and fault behavior. Besides, high fluid viscosity under the same fluid pressure magnitude is found to be favorable of unstable slip suggested by the decreasing trend of friction rate parameter (a-b) from positive to negative (Cornelio and Violay, 2020a). Given the complexity of the variation in friction rate parameter (a-b), future studies on the pore pressure effect on friction rate parameter (a-b) are suggested to be conducted under site-specific conditions. Moreover, since the effective normal stress has been changing during fluid injection, studying the evolution of fault friction through effective-normal-stress-stepping tests could also be an avenue to provide more clues to the injection-induced fault response (Kilgore et al., 2017; Linker and Dieterich, 1992; Shreedharan et al., 2019).

Transient changes in pore pressure caused by shear-induced dilatancy or compaction during ongoing shear also have great impacts on the frictional behavior of faults. Samuelson et al. (2009) estimate the dilatancy coefficient of quartz gouge obtained from velocity-stepping tests (1 to 100 μm/s) under effective normal stresses ranging from 0.8 to 20 MPa. They find that the dilatancy coefficient is independent of the effective normal stress and increasing shear strain. They numerically model the dilatant hardening caused by dilatancy-induced depressurization under seismogenic conditions and find that this process could potentially arrest the unstable fault slip. Recently, Faulkner et al. (2017) find that the pore pressure increase induced by shear-enhanced compaction of low-permeable gouge has a great influence on laboratory frictional measurements, including frictional strength, RSF friction parameters, and slide-hold-slide results. More lately, Proctor et al. (2020) show that the dilatancy-induced pore pressure reduction delays the slow slip of a bare fault in Westerly granite, while the raised pore pressure on a gouge-filled fault advances the dynamic fault slip due to gouge compaction. However, the transient change of pore pressure prior to injection-induced fault slip is unknown and how it influences the injection-induced fault behavior remains poorly understood.

Dynamic weakening mechanisms can also be changed by different physical states and properties of fluid. As an example, flash heating, as a dominant mechanism for dynamic fault weakening during co-seismic slip under high normal stresses, is likely prohibited in injection-induced fault slip because the delayed water phase transition of high-pressure water can buffer the temperature buildup required to activate flash heating (Acosta et al., 2018). The SEM image of a sawcut fault surface after injection-induced dynamic slip directly corroborates the inhibition of flash heating with the presence of high-pressure water (Ji and Wu, 2020), because there are no melted structures. Generally, this heat buffer effect is dependent on fluid pressure, as well as compressibility, thermal diffusivity, density, and viscosity of fluid (Acosta et al., 2018). Among them, the fluid viscosity is a decisive parameter in controlling the fault weakening mechanism of laboratory earthquakes, and only slightly reduces the static fault friction for reactivation (Cornelio et al., 2019). In particular, during fault weakening, flash heating is active in low viscosity fluid, such as water, while this mechanism is suppressed, and elasto-hydrodynamic lubrication (EHD) becomes dominant with the presence of high viscosity fluid. As shown in Fig. 18 (Cornelio and Violay, 2020b), EHD lubrication is the fully lubrication regime, where the normal stress is fully supported by the fluid pressure when $S > 1$. S is the Sommerfeld number defined as the fluid pressure normalized by the effective normal stress (Brodsky and Kanamori, 2001). When $10^{-3} < S < 1$, the normal stress is collectively supported by solid contacts and fluid pressure in the mixed lubrication regime. If the normal stress is supported by the solid contacts ($S < 10^{-3}$), it is referred to as the boundary lubrication regime. Cornelio et al. (2019) have derived the criterion for the lubrication regimes from laboratory experiments and have found that higher fluid viscosity and lower normal stress increase the efficiency of EHD. EHD is found as an effective weakening mechanism during natural and anthropogenic earthquakes (Cornelio and Violay, 2020b). In the injection-driven shear tests, fluid with higher viscosity takes more time to diffuse along the fault (Passelègue et al., 2018) and can result in a higher fluid overpressure ratio, and moreover the presence of high viscosity fluid promotes shear-induced compaction (Cornelio and Violay, 2020a), collectively increasing the likelihood and magnitude of injection-induced seismicity. However, currently no injection-driven shear tests using fluids with different viscosity have yet been reported, which are expected to provide supplementary results to further understand the effect of fluid viscosity on injection-induced seismicity.

As opposed to the macroscale fluid lubrication model, AFM provides an avenue to investigate the micro-physical mechanisms of water lubrication. For instance, Dou et al. (2020) show that a nanometer-thick water layer forms on the granite surface, reducing the shear force by shifting the shear plane from granite/granite interface to water layer. Diao and Espinosa-Marzal (2018) carry out a more comprehensive study on the role of water on fault lubrication using AFM. They find three different regimes of water lubrication on a single planar calcite (Fig. 19), including viscous shear and hydration lubrication, shear-promoted thermally activated slip, and pressure solution facilitated slip at low, intermediate, and higher normal stresses, respectively. Their work demonstrates that a lubricating film exists between the calcite and silica (AFM tip) interface. The pressure solution at slow sliding velocities under high normal stresses is potentially responsible for the fault weakening at the scale of asperity contact. As a line of direct evidence,

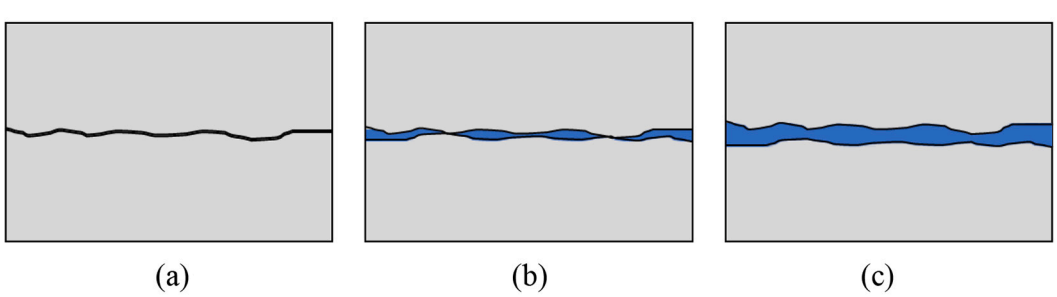

Fig. 18. Three different fluid lubrication regimes on a single fault (replotted from Cornelio and Violay, 2020b). (a) Boundary lubrication ($S < 10^{-3}$). (b) Mixed lubrication ($10^{-3} < S < 1$). (c) Elasto-hydrodynamic (EHD) lubrication ($S > 1$). S is the Sommerfeld number.

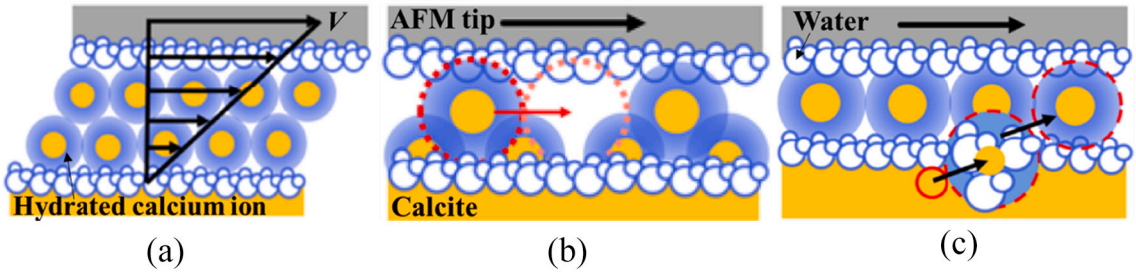

Fig. 19. Three different friction mechanisms identified by nanoscale displacement-driven shear tests on an atomically flat calcite plane in an aqueous environment at (a) low normal stress: viscous flow, (b) intermediate normal sterss: thermally activated slip, and (c) high normal stress: pressure solution facilitaed sliding (Diao and Espinosa-Marzal, 2018).

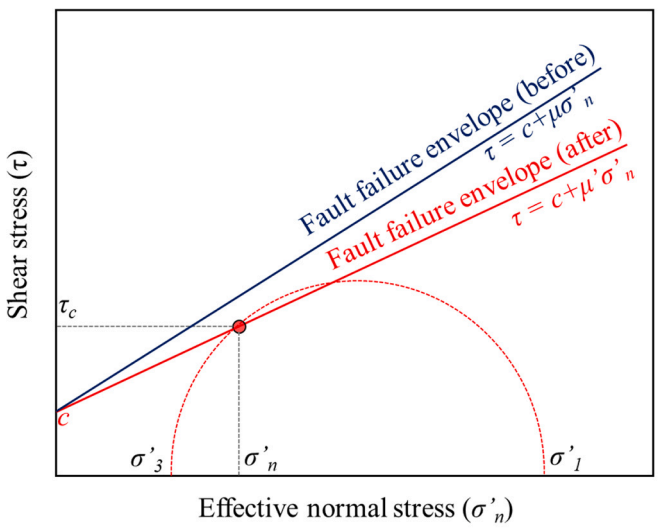

Fig. 20. Schematic diagram showing the reactivation of a critically stressed fault by water lubrication. σ'_1 and σ'_3 are the maximum and minimum effective principal stresses, respectively. σ'_n and τ_c are the effective normal stress and critically stress on the fault, respectively. c is the cohesion of the fault. The reduction of friction coefficient from μ to μ' caused by water lubrication leads to the reactivation of the critically stressed fault.

Dou et al. (2020) experimentally demonstrate that a critically stressed fault in granite can be induced to slip solely by water lubrication (Fig. 20), in which the reduction in friction coefficient rotates the failure envelope to tough the stress state (represented by red point) of the fault.

4.5. Effect of fluid chemistry

In this section, we focus on the chemical interactions between fault and fluid, such as mineral dissolution and precipitation (Ma et al., 2020, 2021), in addition to the physical mechanisms leading to injection-induced fault slip. The pH environment has a profound impact on the frictional strength and shear stiffness of rock faults (Nouailletas et al., 2017; Shang et al., 2020). The treatment of faults in carbonate rock using the acid solution of pH = 0.2 has a negligible influence on the fault surface roughness, while the mechanical properties have been greatly impacted by the acid treatment (Nouailletas et al., 2017). Specifically, the frictional strength and shear stiffness both reduces with a decreased dilation angle due to the weakening of faults. For faults in granite, the solution of pH = 2 reduces the frictional strength and shear stiffness more significantly, compared to the solution of pH = 12 (Shang et al., 2020). This is because there is only dissolution of minerals in acid solutions, while dissolution and precipitation of minerals compete in alkaline solutions. Mineral dissolution has been speculated to have an influence on the 2017 M_w 5.5 Pohang Earthquake, South Korea. In particular, a careful examination of the flowback water from the 4215 m deep PX-1 borehole, following the August 2017 hydraulic stimulation of a granodiorite geothermal reservoir in Pohang, suggests that quartz dissolution by water injection is active in the field, potentially resulting in the fault strength reduction (Burnside et al., 2019). Mineral precipitation has been extensively studied in the laboratory (e.g., Jones and Detwiler, 2016), and its effect on injection-induced seismicity is twofold (Yarushina and Bercovici, 2013). On the one hand, the permeability reduction associated with mineral precipitation leads to a larger fluid overpressure ratio and thereby encourages a larger injection-induced seismic moment (Fig. 13). On the other hand, mineral carbonation in CO_2 sequestration sites consumes the fluids and thus reduces the pore pressure significantly. Moreover, the increase in grain contact area due to carbonation reaction allows the distribution of load on the fault, reducing the stress magnitude. In this way, the injection-induced seismicity can be mitigated by mineral precipitation in CO_2 sequestration sites (Yarushina and Bercovici, 2013). Sometimes, chemical interactions are not active or have no short-term impact on the fault behavior. In the background of CO_2 storage, Samuelson and Spiers (2012) demonstrate that the addition of supercritical CO_2 to dry and to brine saturated fault gouges, prepared from the caprock and reservoir rock obtained near a potential CO_2 storage site in the Netherland, does not change the frictional strength. This finding is consistent with the results obtained more recently by Zhang et al. (2019b). Moreover, either the addition of brine or supercritical CO_2 has no obvious influence on the friction rate parameter (a-b). These results suggest that the short-term effect of supercritical CO_2 on fault reactivation is negligible and that faults in these rocks are intrinsically aseismic. The chemical composition and pH environment are also important in fault lubrication. As an example, in the nanoscale using AFM, Diao and Espinosa-Marzal (2019) find that NaCl solutions reduce the friction coefficient of a planar calcite under low normal stresses more efficiently than $CaCl_2$. On the other hand, $CaCl_2$ solutions promote the fault weakening more significantly than NaCl when pressure solution is active at slow sliding velocities under high normal stresses, possibly due to the lower reactivity of calcite in the higher pH environment.

In addition, acid stimulation is a promising method to improve the well productivity in deep geothermal reservoirs while maintain a low seismic rate through injecting acidified water. This has been proved in the Soultz-sous-Forêts EGS field (France) (Calò et al., 2014; Lucas et al., 2020). The dissolution of carbonates in acid stimulation may help to create rougher fault surfaces compared to conventional hydraulic stimulation (Portier et al., 2009; Shang et al., 2020). As presented in Section 4.1, the injection-induced response of rougher faults is aseismic (Fig. 10), which could be a possible explanation for the observed reduction of seismic rates in acid stimulation (Ji and Wu, 2020). However, the underlying hydro-chemo-mechanical mechanism remains enigmatic. Future investigation on the behavior of critically stressed faults in various rocks driven by acidified water injection may be able to provide some more valuable insights.

4.6. Effect of injection protocol

Designing a controlled injection protocol can possibly reduce injection-induced seismic risks. Thus, it is valuable to characterize the fault responses to different injection protocols in laboratory experiments. The most straightforward parameter involved in injection design is the rate of fluid injection (either volumetric flow rate or pressurization rate). As already discussed in Section 4.2, under locally undrained condition, a faster injection rate can result in a larger fluid overpressure ratio and thereby a faster rupture velocity and a larger seismic moment (Fig. 13). Similarly, under fully drained condition, fluid injection at a faster injection rate into a fault in a highly permeable sandstone promotes dynamic and unstable fault slip (Wang et al., 2020b) and a faster rate of seismic moment release (Wang et al., 2020a). Specifically, the cumulative seismic moment scales with the cube of injected volume during dynamic slip, while during stable slip the relationship between cumulative seismic moment and injected volume becomes linear (Fig. 21). Therefore, the transition from linear relation to cubic relation between cumulative seismic moment and injected volume could probably serve as a sign of transition from stable to dynamic slip. In addition, the seismic moment release recorded by the AE system accounts for an extremely small fraction of that calculated from shear displacement, indicating that injection-induced seismic moment release is mostly aseismic. In any case (i.e., locally undrained, or fully drained), keeping a slow injection rate is helpful to reduce the injection-induced seismic risks.

In addition to the effect of injection rate, optimizing the injection strategy is also essential to reduce the injection-induced seismic risks. Cyclic injection strategies have been proposed as a potential solution to efficient permeability enhancement and seismic risk mitigation (Hofmann et al., 2018, 2019; Zang et al., 2013, 2019; Zhuang and Zang, 2021). However, whether cyclic injection is effective in mitigating injection-induced seismic risks remains highly debated in terms of various fault responses to cyclic injection reported in different experimental studies. According to Noël et al. (2019), the displacement-driven fault slip changes from stable slip to unstable slip under cyclic fluid pressurization, which means cyclic injection encourages the occurrence of seismic events. They ascribe this transition to the enhanced critical stiffness of fault (k_c in Eq. (4)) due to slip perturbation caused by cyclic pressurization. In contrast, cyclic injection can reduce the fluid overpressure ratio and thereby the resulting maximum seismic moment on critically stressed sawcut faults in granite (Fig. 22, Ji et al., 2021b).

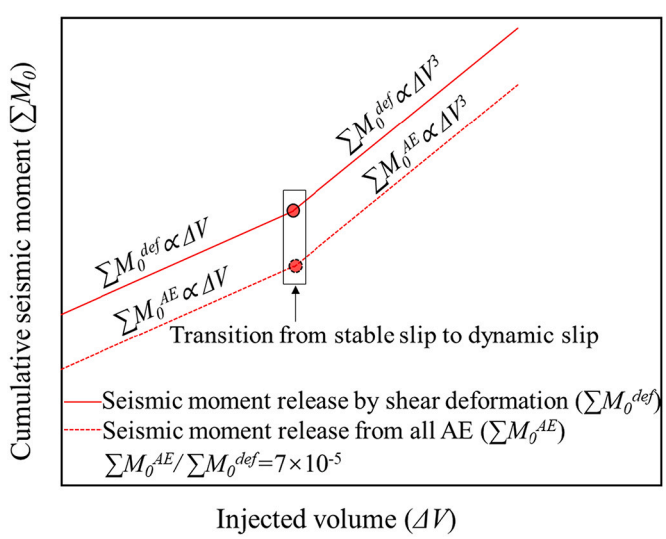

Fig. 21. Cumulative seismic moment as a function of injected volume in fast dynamic slip and slow stable slip (plotted based on Wang et al. (2020a)). The transition from a linear relation to a cubic relation between cumulative seismic moment and injected volume can be a signal of the shift from stable slip to dynamic slip. The extremely small ratio between seismic moment release calculated from AE to that from shear deformation suggests that aseismic deformation accounts for a large portion of total seismic moment release.

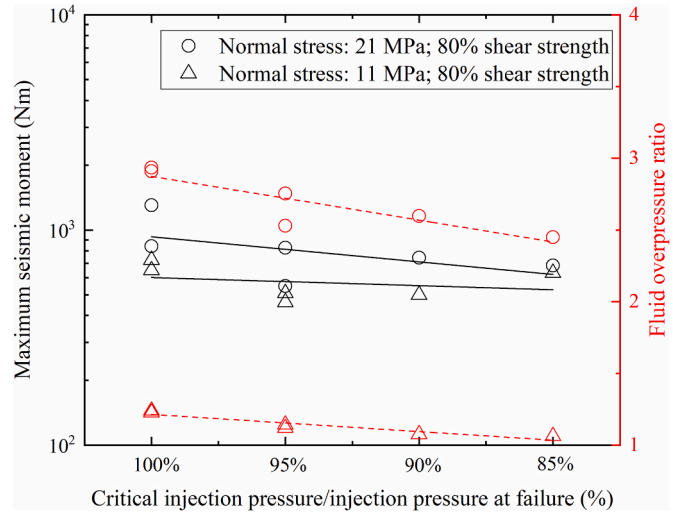

Fig. 22. Maximum seismic moment and fluid overpressure ratio as a function of critical injection pressure (replotted based on the data in Ji et al. (2021b)). 100% represents the monotonic injection case.

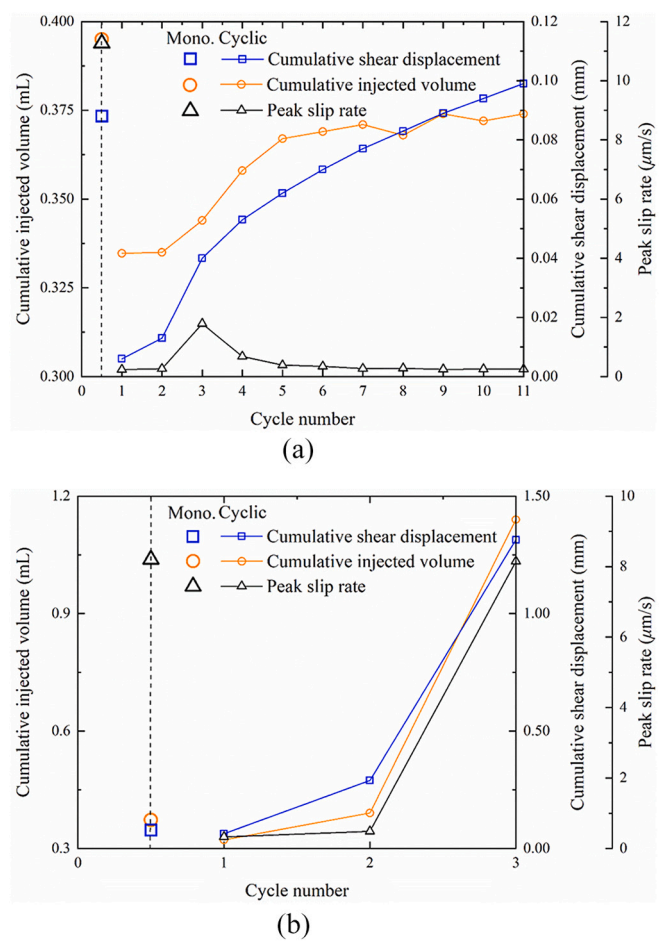

Fig. 23. Cumulative injected volume, cumulative shear displacement and peak slip rate as a function of cycle number in the (a) pressure-controlled monotonic (Mono.) and cyclic fluid injection tests and (b) volume-controlled monotonic (Mono.) and cyclic fluid injection tests (Ji et al., 2021d).

Moreover, Ji et al. (2021d) find that cyclic injection also seems to be effective in mitigating injection-induced seismic risks on a natural fault in granite by promoting slow and stable slip (Fig. 23). This is due to the constrained peak injection pressure and the subsequent flowback or diffusion of fluid pressure. However, reinjection after an unstable shut-in period signified by an unusual pressure drop cannot guarantee slow fault slip anymore (cycle 3 in Fig. 23b). The contradictory conclusions reached by Noël et al. (2019) and Ji et al. (2021b, 2021d) are primarily due to the drainage condition of the fault. This also suggests that the injection design must be tailored for specific purposes and that there is lots of room for improvement and optimization. A more comprehensive study on the fault behavior during cyclic injection spanning from undrained to drained conditions is expected in the future.

5. Summary of recent advances

The above review suggests that important physical and chemical mechanisms of injection-induced seismicity have been revealed from previous experimental studies. Here, we outline some important recent advances gained from previous laboratory studies in terms of the effects of fault properties, stress state, temperature, fluid physics, fluid chemistry and injection protocol.

(1) *Effect of fault properties.* The effect of fault properties on fault behavior, primarily including fault roughness and minerology, has long been recognized and comprehensively investigated (Dieterich, 1978, 1979; Tembe et al., 2010; Kohli and Zoback, 2013). Under simplified laboratory conditions, compared to smooth faults, the preparatory process on rough faults is more likely to be aseismic (Dresen et al., 2020) and the magnitude of stick-slip failure along rough faults is smaller primarily due to the heterogeneous local stress field as revealed by the high-resolution AE hypocenter locations (Goebel et al., 2017). Injection-driven slip along rough faults is aseismic in contrary to the injection-driven seismic slip along smooth faults (Ji and Wu, 2020). Similar to the displacement-driven fault slip, the injection-driven fault slip may be also presumably controlled by the local stress distribution, and a higher applied normal stress may promote seismic behavior irrespective of the fault roughness (Ye and Ghassemi, 2018). Besides, rough faults are characterized by a higher friction coefficient and stronger velocity-strengthening behavior (Fang et al., 2018a). Cumulative asperity damage causes the transition from velocity-strength, to velocity-neutral and finally to velocity-weakening behavior on both smooth and rough faults. The permeability evolution along faults undergoing shear is complicated by the normal stress, asperity height, slip velocity and shear displacement (Ishibashi et al., 2018; Shen et al., 2020). The presence of clay minerals reduces the friction coefficient and promotes velocity-strengthening behavior due to the clay supported grain-packing framework (Fang et al., 2017, 2018b; Kohli and Zoback, 2013; Ikari et al., 2009; Wang et al., 2019). Injection-driven fault slip is collectively controlled by the evolving hydraulic properties, and rate-and-state frictional properties of faults (Scuderi and Collettini, 2018). The injection-induced dynamic slip along intrinsically velocity-strengthening faults is caused by the overwhelming fault weakening due to significant pore pressure increase (Scuderi et al., 2017). The complex evolution of the permeability of a fault (Okazaki et al., 2013; Kluge et al., 2021) may further complicate the diffusion of fluid in the fault and thereby the occurrence of injection-induced seismicity.

(2) *Effect of stress state.* The displacement-driven shear tests under various stresses suggest that aseismic deformation is favored in most reservoir conditions (Kilgore et al., 1993; Scholz, 1998; Scuderi et al., 2017), which is in direct contradiction to the current observations that most injection-induced earthquakes are confined to the upper crust. This contradiction suggests the necessity of conducting injection-driven shear tests. Based on the studies on injection-driven slip on favorably oriented faults in granite (Ji and Wu, 2020; Ji et al., 2021a; Passelègue et al., 2018, 2020), we may conclude that higher stress magnitudes generally increase the magnitude of injection-induced seismic events, presumably due to the larger fluid overpressure ratio and larger magnitude of stored elastic energy in the sample-testing machine system, a proxy for the fault-surrounding rock system in the field. In addition, melt welding (Hayward and Cox, 2017) and stress rotation (Giorgetti et al., 2019) have been proven to play significant roles in controlling the displacement-driven slip behavior of unfavorably oriented faults in the ambient stress filed.

(3) *Effect of temperature.* Aseismic fault behavior appears to be favored by high temperature due to the transition of fault rheology from brittle to ductile (Brace and Byerlee, 1970; Paterson and Wong, 2005; Scholz, 1998) and active fluid-assisted deformation processes (Blanpied et al., 1995), while the fault permeability reduction associated with thermal-assisted processes (Polak et al., 2003; Yasuhara et al., 2004; Blöcher et al., 2016) promotes heterogeneous fluid pressure distribution and thereby a larger seismic moment (Ji and Wu, 2020). Thermal stress caused by colder water injection into a hot fault is proven to be able to drive aseismic fault creep before injection-induced fault reactivation, and in the post-hydro-shearing stage, high temperature promotes fracture closure by causing asperity degradation and mineral dissolution (KC and Ghazanfari, 2021). Besides, the transient high temperature generated during dynamic fault slip may contribute to the dynamic fault weakening by mechanisms such as thermal pressurization (Rice, 2006), flash heating (Acosta et al., 2018) and thermal dehydration of clay minerals (Ujiie and Tsutsumi, 2010).

(4) *Effect of fluid physics.* With the presence of water, gouge grain contact area could be increased due to active water-assisted processes during fault dynamic instability, resulting in a larger stick-slip friction drop and a faster frictional healing rate (Scuderi et al., 2014). The change of friction rate parameter (a-b) with increasing pore pressure and increasing fluid viscosity shows diverse trends (Scuderi and Collettini, 2016; Xing et al., 2019; Cornelio and Violay, 2020a), depending on many factors, such as effective stress, porosity, strain rate and mineralogy of fault gouge, and thus the characterization of this change should be conducted under site-specific conditions. Besides, the transient pore pressure change greatly influences the onset, propagation, and magnitude of displacement-driven dynamic fault slip (Samuelson et al., 2009; Faulkner et al., 2017; Proctor et al., 2020). The fluid viscosity has been demonstrated as a critical parameter controlling the dynamic weakening mechanisms of fault through changing the Sommerfeld number and the macroscope lubrication regimes (Acosta et al., 2018; Cornelio et al., 2019; Cornelio and Violay, 2020b). The elasto-hydrodynamic lubrication (EHD) is proposed as the dominant weakening mechanism in natural and induced earthquakes (Cornelio and Violay, 2020b). In the microscale, there are three different regimes of water lubrication on a single planar calcite depending on the normal stress and slip velocity revealed by AFM measurements, which can also be influenced by the fluid chemistry (Diao and Espinosa-Marzal, 2018). Fault lubrication caused by water, as one of the mechanisms of injection-induced seismicity, can independently drive a critically stressed fault in granite to slip (Dou et al., 2020).

(5) *Effect of fluid chemistry.* The pH of fluid can cause mineral dissolution or precipitation, modifying the fault behavior by changing the frictional strength and shear stiffness (Nouailletas et al., 2017; Shang et al., 2020). Mineral dissolution reduces the frictional strength of faults in granite, potentially promoting injection-induced fault slip (Burnside et al., 2019). However, mineral

precipitation has a twofold influence on injection-induced seismicity. It can reduce the reservoir permeability and increase the degree of fluid pressure heterogeneity, possibly resulting in a larger seismic moment release (Ji and Wu, 2020). On the contrary, the stress magnitude can decrease with increasing grain contact area due to mineral precipitation, thus likely reducing the seismic risks (Yarushina and Bercovici, 2013). The supercritical CO_2 and brine saturated conditions do not influence much the frictional strength and friction rate parameter *(a-b)* in the short-term (Samuelson and Spiers, 2012; Zhang et al., 2019). In addition, fault lubrication is shown to be also dependent on the chemical compositions of fluid and fault and pH environment (Diao and Espinosa-Marzal, 2019).

(6) *Effect of injection protocol.* Regarding the injection rate, a slow slip rate and a slow seismic moment release rate during injection-induced fault slip can be encouraged by a low fluid pressurization rate (Wang et al., 2020a, 2020b). Cyclic injection has been shown to promote fault instability (Noël et al., 2019) and to suppress fault instability (Ji et al., 2021b, 2021d) in different laboratory studies. The contradictory results on fault stability subject to cyclic injection are primarily attributed to the different drainage conditions of the fault (Ji et al., 2021b, 2021d; Noël et al., 2019). The current results on the effect of cyclic injection on fault stability indicate an urgent need to further constrain the injection parameters based on the reservoir conditions.

6. Open questions and future perspectives

Despite the vast advances on the understanding of injection-induced seismicity obtained from previous laboratory experiments, a number of important scientific questions remain to be answered. Here, we highlight the key areas for next frontiers of experimental studies on injection-induced seismicity.

(1) *Assessing competing propagation of pressure and rupture fronts in heterogeneous faults with complex architecture.* Future work is expected to reveal how a critically stressed heterogeneous fault with complex fault architecture is reactivated by fluid injection. The experiment should be conducted under undrained condition, which is more suitable for simulating injection-induced seismicity extending beyond the stimulated volume (i.e., the most dangerous case in which larger magnitude earthquakes may occur). It is useful to quantify concurrently the fault rupture front and fluid pressure front on such a heterogeneous fault to identify the transition from arrested to runaway rupture and adapt the injection strategy accordingly to mitigate the seismic risks. Technically, the fault rupture front has been successfully estimated from strain gauge array and acoustic records (Passelègue et al., 2020). Fiber optic pressure sensors (Blöcher et al., 2014; Ji et al., 2022; Nicolas et al., 2020; Reinsch et al., 2012) are promising in tracking the fluid pressure front during injection-driven shear tests. This idea attempts to adapt the injection strategy to mitigate seismic events based on the seismic and hydraulic monitoring data. If this is achieved in the laboratory, it can not only improve our understanding on arrest-runaway rupture transition, but also provide a laboratory demonstration for the concept of seismic-informed adaptive injection strategy in the field scale.

(2) *Understanding the mechanisms of injection-induced reactivation of unfavorably oriented faults.* To the best of our knowledge, no injection-driven shear tests have been carried out on misoriented faults so far. It thus remains unclear as to how a critically stressed and unfavorably oriented fault responds to fluid injection with the involvements of processes such as melt welding (Hayward and Cox, 2017) and stress rotation (Giorgetti et al., 2019). Thus, injection-induced reactivation of misoriented faults needs future investigation.

(3) *Revealing the thermal effect on colder water injection-induced slip of hot faults for EGS settings.* Most injection-driven shear tests have been performed under room temperature, which cannot represent the real thermal conditions in the subsurface. Colder fluid injection into a critically stressed fault under hydrothermal conditions could provide more pertinent evidence for the injection-induced fault behavior under deep reservoir conditions, especially in EGS.

(4) *Quantifying the transient pore pressure change during injection-driven fault slip.* The significant role of transient pore pressure change in displacement-driven shear tests has been identified in many laboratory studies (Samuelson et al., 2009; Faulkner et al., 2017; Proctor et al., 2020). A direct measurement of transient pore pressure changes during the injection-driven fault slip is desirable to better understand how transient change in pore pressure contributes to injection-induced fault slip.

(5) *Exploring the fault slip behavior subject to direct injection of fluid with different viscosity and chemistry.* Although the effects of fluid viscosity and chemistry on fault behavior have been revealed to some degree by performing displacement-driven shear tests, the dynamic processes accompanying the direct injection of fluid with different viscosity and pH to a critically stressed fault remain enigmatic. This necessitates further exploration of the effects of fluid viscosity and chemistry on injection-induced seismicity.

(6) *Understanding the slip transition induced by different injection schemes accompanying undrained-drained transition.* Future investigation on fault slip behavior under undrained-drained transition promoted by different injection schemes could refine the injection designs for better management of injection-induced seismicity. Particularly, this can also help to reconcile the current opposite findings on the effect of cyclic injection on injection-induced seismic risks reported by Ji et al. (2021b, 2021d) and Noël et al. (2019).

(7) *Upscaling based on multiscale experiments.* Even though laboratory studies have greatly furthered our understanding on injection-induced seismicity in geoenergy systems, the limitation of laboratory study is obvious especially in terms of the finite sample dimensions (normally in centimeter scale). One way to compensate for this limitation is to use larger samples in meter scale in the injection-driven shear test (e.g., Cebry and McLaskey, 2021) in the laboratory. Another way forward is to conduct mine scale fluid injection experiments in decameter scale (e.g., Guglielmi et al., 2015; Zang et al., 2017), in which a more realistic simulation of the field scale can be achieved. The combination of these centimeter, meter, and decameter experiments could future constrain the processes causing injection-induced seismicity for better management and effective mitigation of the seismic risks in geoenergy systems.

7. Conclusions

Injection-induced seismicity has been receiving increasing attention in recent years. In this review, we provide a timely, comprehensive, and critical review of laboratory experiments on fault behavior aiming at deciphering the mechanisms of injection-induced seismicity. The basics of fault behavior is first reviewed, followed by the introduction of typical experimental setups, and details of the sample preparation, fluid pathway and stress state in triaxial shear-flow setups with some auxiliary techniques. Our review focuses on the effects of fault properties, stress state, temperature, fluid physics, fluid chemistry, and injection protocol on injection-induced fault behavior. We notice that there is a paucity of injection-driven shear tests compared to the displacement-driven shear tests in the literature. These previous experimental studies collectively provide valuable insights into how multiple factors

affect the injection-induced fault stability and seismic responses. Nevertheless, the coupled thermo-hydro-mechanical-chemical processes underpinning injection-induced seismicity are far more complex than the simplified experimental conditions. The next frontier of laboratory experiments is to simulate the injection-induced fault slip under more realistic reservoir conditions, particularly considering the heterogeneity, orientation, temperature, and drainage of the fault as well as the viscosity and chemistry of the fluid.

Credit author statement

Yinlin Ji: Conceptualization and original draft preparation; Hannes Hofmann: Writing-review and editing; Kang Duan: Writing-review and editing; Arno Zang: Writing-review and editing. All authors discussed the content, reviewed, edited the manuscript and ultimately agreed to the submitted version of the manuscript.

Declaration of Competing Interest

The authors declare no conflict of interest.

Acknowledgements

This review would not be possible without Yinlin Ji's four years (2016–2020) of Ph. D. research on injection-induced seismicity in Nanyang Technological University (NTU), Singapore. Thus, the first author greatly acknowledges the NTU Ph. D. Research Scholarship. This work has also been supported by the Helmholtz Association's Initiative and Networking Fund for the Helmholtz Young Investigator Group ARES (contract number VH-NG-1516). The authors are also grateful for the financial support provided by the "Kennis Effecten Mijnbouw" (KEM)-programme through the project "Risk of seismicity due to cooling effects in geothermal systems-KEM-15", and input from Staatstoezicht op de Mijnen (SodM, Dutch State Supervision on Mines). We are grateful to the authors of all the literature cited in this paper, who devoted themselves to better understanding of injection-induced seismicity.

References

Acosta, M., Passelègue, F.X., Schubnel, A., Violay, M., 2018. Dynamic weakening during earthquakes controlled by fluid thermodynamics. Nat. Commun. 9 (1), 3074.
Acosta, M., Passelègue, F.X., Schubnel, A., Madariaga, R., Violay, M., 2019. Can precursory moment release scale with earthquake magnitude? A view from the laboratory. Geophys. Res. Lett. 46, 12927–12937.
Almakari, M., Chauris, H., Passelègue, F., Dublanchet, P., Gesret, A., 2020. Fault's hydraulic diffusivity enhancement during injection induced fault reactivation: application of pore pressure diffusion inversions to laboratory injection experiments. Geophys. J. Int. 223 (3), 2117–2132.
Aubry, J., Passelègue, F., Deldicque, D., Girault, F., Marty, S., Lahfid, A., Bhat, H., Escartin, J., Schubnel, A., 2018. Frictional heating processes and energy budget during laboratory earthquakes. Geophys. Res. Lett. 45 (22), 12274–12282.
Bao, X., Eaton, D.W., 2016. Fault activation by hydraulic fracturing in western Canada. Science 354 (6318), 1406–1409.
Beeler, N., Tullis, T., Blanpied, M., Weeks, J., 1996. Frictional behavior of large displacement experimental faults. J. Geophys. Res. Solid Earth. 101 (B4), 8697–8715.
Bhattacharya, P., Viesca, R.C., 2019. Fluid-induced aseismic fault slip outpaces pore-fluid migration. Science 364 (6439), 464–468.
Blanpied, M.L., Lockner, D.A., Byerlee, J.D., 1995. Frictional slip of granite at hydrothermal conditions. J. Geophys. Res. 100 (B7), 13045–13064.
Blanpied, M.L., Tullis, T.E., Weeks, J.D., 1998. Effects of slip, slip rate, and shear heating on the friction of granite. J. Geophys. Res. Solid Earth 103 (B1), 489–511.
Blöcher, G., Reinsch, T., Hassanzadegan, A., Milsch, H., Zimmermann, G., 2014. Direct and indirect laboratory measurements of poroelastic properties of two consolidated sandstones. Int. J. Rock Mech. Min. Sci. 67, 191–201.
Blöcher, G., Reinsch, T., Henninges, J., Milsch, H., Regenspurg, S., Kummerow, J., Francke, H., Kranz, S., Saadat, A., Zimmermann, G., Huenges, E., 2016. Hydraulic history and current state of the deep geothermal reservoir Groß Schönebeck. Geothermics 63, 27–43.
Brace, W., Byerlee, J., 1966. Stick-slip as a mechanism for earthquakes. Science 153 (3739), 990–992.
Brace, W., Byerlee, J., 1970. California earthquakes: why only shallow focus? Science 168 (3939), 1573–1575.
Brodsky, E.E., Kanamori, H., 2001. Elastohydrodynamic lubrication of faults. J. Geophys. Res. 106 (B8), 16357–16374.
Brown, M.R., Ge, S., 2018. Distinguishing fluid flow path from pore pressure diffusion for induced seismicity. Bull. Seismol. Soc. Am. 108 (6), 3684–3686.
Buijze, L., Guo, Y., Niemeijer, A.R., Ma, S., Spiers, C.J., 2021. Effects of heterogeneous gouge segments on the slip behavior of experimental faults at dm scale. Earth Planet. Sci. Lett. 554, 116652.
Burnside, N.M., Westaway, R., Banks, D., Zimmermann, G., Hofmann, H., Boyce, A.J., 2019. Rapid water-rock interactions evidenced by hydrochemical evolution of flowback fluid during hydraulic stimulation of a deep geothermal borehole in granodiorite: Pohang, Korea. Appl. Geochem. 111.
Byerlee, J.D., 1967. Frictional characteristics of granite under high confining pressure. J. Geophys. Res. 72 (14), 3639–3648.
Byerlee, J.D., Savage, J.C., 1992. Coulomb plasticity within the fault zone. Geophys. Res. Lett. 19 (23), 2341–2344.
Calò, M., Dorbath, C., Frogneux, M., 2014. Injection tests at the EGS reservoir of Soultz-sous-Forêts. Seismic response of the GPK4 stimulations. Geothermics 52, 50–58.
Cappa, F., Guglielmi, Y., Nussbaum, C., Birkholzer, J., 2018. On the relationship between fault permeability increases, induced stress perturbation and the growth of aseismic slip during fluid injection. Geophys. Res. Lett. 45 (20), 11,012–11,020.
Cebry, S.B.L., McLaskey, G.C., 2021. Seismic swarms produced by rapid fluid injection into a low permeability laboratory fault. Earth Planet. Sci. Lett. 557, 116726.
Chen, J., Niemeijer, A.R., Spiers, C.J., 2017. Microphysically derived expressions for rate-and-state friction parameters, a, b, and Dc. J. Geophys. Res. 122 (12), 9627–9657.
Collettini, C., Di Stefano, G., Carpenter, B., Scarlato, P., Tesei, T., Mollo, S., Trippetta, F., Marone, C., Romeo, G., Chiaraluce, L., 2014. A novel and versatile apparatus for brittle rock deformation. Int. J. Rock Mech. Min. Sci. 66, 114–123.
Collettini, C., Tesei, T., Scuderi, M.M., Carpenter, B.M., Viti, C., 2019. Beyond Byerlee friction, weak faults and implications for slip behavior. Earth Planet. Sci. Lett. 519, 245–263.
Cornelio, C., Violay, M., 2020a. Effect of fluid viscosity on earthquake nucleation. Geophys. Res. Lett. 47 (12).
Cornelio, C., Violay, M., 2020b. Parametric analysis of the elastohydrodynamic lubrication efficiency on induced seismicity. Geophys. J. Int. 222 (1), 517–525.
Cornelio, C., Spagnuolo, E., Di Toro, G., Nielsen, S., Violay, M., 2019. Mechanical behaviour of fluid-lubricated faults. Nat. Commun. 10 (1), 1–7.
Cornelio, C., Passelègue, F.X., Spagnuolo, E., Di Toro, G., Violay, M., 2020. Effect of fluid viscosity on fault reactivation and coseismic weakening. J. Geophys. Res. 125 (1).
Dahm, T., Cesca, S., Hainzl, S., Braun, T., Krüger, F., 2015. Discrimination between induced, triggered, and natural earthquakes close to hydrocarbon reservoirs: a probabilistic approach based on the modeling of depletion-induced stress changes and seismological source parameters. J. Geophys. Res. 120 (4), 2491–2509.
Di Toro, G., Hirose, T., Nielsen, S., Pennacchioni, G., Shimamoto, T., 2006. Natural and experimental evidence of melt lubrication of faults during earthquakes. Science 311 (5761), 647–649.
Diao, Y., Espinosa-Marzal, R.M., 2018. The role of water in fault lubrication. Nat. Commun. 9 (1), 1–10.
Diao, Y., Espinosa-Marzal, R.M., 2019. Effect of fluid chemistry on the interfacial composition, adhesion and frictional response of calcite single crystals-implications for injection-induced seismicity. J. Geophys. Res. 124 (6), 5607–5628.
Dieterich, J.H., 1972. Time-dependent friction in rocks. J. Geophys. Res. 77 (20), 3690–3697.
Dieterich, J.H., 1978. Time-dependent friction and the mechanics of stick-slip. Pure Appl. Geophys. 116 (4–5), 790–806.
Dieterich, J.H., 1979. Modeling of rock friction: 1. Experimental results and constitutive equations. J. Geophys. Res. 84 (B5), 2161–2168.
Dou, Z., Gao, T., Zhao, Z., Li, J., Yang, Q., Shang, D., 2020. The role of water lubrication in critical state fault slip. Eng. Geol. 271.
Dresen, G., Kwiatek, G., Goebel, T., Ben-Zion, Y., 2020. Seismic and aseismic preparatory processes before large stick–slip failure. Pure Appl. Geophys. 1–20.
Eaton, D.W., Igonin, N., 2018. What controls the maximum magnitude of injection-induced earthquakes? Lead. Edge 37 (2), 135–140.
Ellsworth, W.L., 2013. Injection-induced earthquakes. Science 341 (6142), 1225942.
Elsworth, D., Spiers, C.J., Niemeijer, A.R., 2016. Understanding induced seismicity. Science 354 (6318), 1380–1381.
Esaki, T., Du, S., Mitani, Y., Ikusada, K., Jing, L., 1999. Development of a shear-flow test apparatus and determination of coupled properties for a single rock joint. Int. J. Rock Mech. Min. Sci. 36 (5), 641–650.
Fang, Y., Elsworth, D., Wang, C., Ishibashi, T., Fitts, J.P., 2017. Frictional stability-permeability relationships for fractures in shales. J. Geophys. Res. 122 (3), 1760–1776.
Fang, Y., Elsworth, D., Ishibashi, T., Zhang, F., 2018a. Permeability evolution and frictional stability of fabricated fractures with specified roughness. J. Geophys. Res. 123, 9355–9375.
Fang, Y., Elsworth, D., Wang, C., Jia, Y., 2018b. Mineralogical controls on frictional strength, stability and shear permeability evolution of fractures. J. Geophys. Res. 123, 3549–3563.
Faulkner, D.R., Jackson, C.A.L., Lunn, R.J., Schlische, R.W., Shipton, Z.K., Wibberley, C. A.J., Withjack, M.O., 2010. A review of recent developments concerning the structure, mechanics and fluid flow properties of fault zones. J. Struct. Geol. 32 (11), 1557–1575.
Faulkner, D.R., Sanchez-Roa, C., Boulton, C., den Hartog, S.A.M., 2017. Pore-fluid pressure development in compacting fault gouge in theory, experiments, and nature. J. Geophys. Res. 123 (1), 226–241.

Foulger, G.R., Wilson, M.P., Gluyas, J.G., Julian, B.R., Davies, R.J., 2017. Global review of human-induced earthquakes. Earth Sci. Rev. 178, 438–514.
Galis, M., Pelties, C., Kristek, J., Moczo, P., Ampuero, J.P., Mai, P.M., 2015. On the initiation of sustained slip-weakening ruptures by localized stresses. Geophys. J. Int. 200 (2), 890–909.
Galis, M., Ampuero, J.P., Mai, P.M., Cappa, F., 2017. Induced seismicity provides insight into why earthquake ruptures stop. Sci. Adv. 3 (12), eaap7528.
Garagash, D.I., Germanovich, L.N., 2012. Nucleation and arrest of dynamic slip on a pressurized fault. J. Geophys. Res. 117 (B10).
Gaucher, E., Schoenball, M., Heidbach, O., Zang, A., Fokker, P.A., van Wees, J.-D., Kohl, T., 2015. Induced seismicity in geothermal reservoirs: a review of forecasting approaches. Renew. Sust. Energ. Rev. 52, 1473–1490.
Giorgetti, C., Tesei, T., Scuderi, M.M., Collettini, C., 2019. Experimental insights into fault reactivation in gouge-filled fault zones. J. Geophys. Res. 124 (4), 4189–4204.
Giorgetti, C., Tesei, T., Scuderi, M.M., Collettini, C., 2019. Experimental Insights into Fault Reactivation in Gouge-filled Fault Zones. J. Geophys. Res. Solid Earth 124 (4), 4189–4204.
Goebel, T.H.W., Kwiatek, G., Becker, T.W., Brodsky, E.E., Dresen, G., 2017. What allows seismic events to grow big?: Insights from b-value and fault roughness analysis in laboratory stick-slip experiments. Geology 45 (9), 815–818.
Grigoli, F., Cesca, S., Rinaldi, A.P., Manconi, A., López-Comino, J.A., Clinton, J.F., Westaway, R., Cauzzi, C., Dahm, T., Wiemer, S., 2018. The November 2017 Mw 5.5 Pohang earthquake: a possible case of induced seismicity in South Korea. Science 360 (6392), 1003–1036.
Guglielmi, Y., Cappa, F., Avouac, J.-P., Henry, P., Elsworth, D., 2015. Seismicity triggered by fluid injection–induced aseismic slip. Science 348 (6240), 1224–1226.
Gutierrez, M., Øino, L.E., Nygård, R., 2000. Stress-dependent permeability of a de-mineralised fracture in shale. Mar. Pet. Geol. 17 (8), 895–907.
Hackston, A., Rutter, E., 2016. The Mohr–Coulomb criterion for intact rock strength and friction – a re-evaluation and consideration of failure under polyaxial stresses. Solid Earth 7 (2), 493–508.
Hardebeck, J.L., Hauksson, E., 1999. Role of fluids in faulting inferred from stress field signatures. Science 285 (5425), 236–239.
Hayward, K.S., Cox, S.F., 2017. Melt welding and its role in fault reactivation and localization of fracture damage in seismically active faults. J. Geophys. Res. 122 (12), 9689–9713.
Hofmann, H., Zimmermann, G., Zang, A., Min, K.-B., 2018. Cyclic soft stimulation (CSS): a new fluid injection protocol and traffic light system to mitigate seismic risks of hydraulic stimulation treatments. Geotherm. Energy 6 (1), 27.
Hofmann, H., Zimmermann, G., Farkas, M., Huenges, E., Zang, A., Leonhardt, M., Kwiatek, G., Martinez-Garzon, P., Bohnhoff, M., Min, K.-B., Fokker, P., Westaway, R., Bethmann, F., Meier, P., Yoon, K.S., Choi, J.W., Lee, T.J., Kim, K.Y., 2019. First field application of cyclic soft stimulation at the Pohang Enhanced Geothermal System site in Korea. Geophys. J. Int. 217 (2), 926–949.
Hubbert, M.K., Rubey, W.W., 1959. Role of fluid pressure in mechanics of overthrust faulting I. Mechanics of fluid-filled porous solids and its application to overthrust faulting. Geol. Soc. Am. Bull. 70 (2), 115–166.
Ikari, M.J., Kopf, A.J., 2011. Cohesive strength of clay-rich sediment. Geophys. Res. Lett. 38 (16).
Ikari, M.J., Saffer, D.M., Marone, C., 2009. Frictional and hydrologic properties of clay-rich fault gouge. J. Geophys. Res. 114 (B5).
Ikari, M.J., Carpenter, B.M., Marone, C., 2016. A microphysical interpretation of rate- and state-dependent friction for fault gouge. Geochem. Geophys. Geosyst. 17 (5), 1660–1677.
Ishibashi, T., Elsworth, D., Fang, Y., Riviere, J., Madara, B., Asanuma, H., Watanabe, N., Marone, C., 2018. Friction-stability-permeability evolution of a fracture in granite. Water Resour. Res. 54, 9901–9918.
Jaeger, J.C., Cook, N.G.W., 1979. Fundamentals of Rock Mechanics, 3rd edn. Chapman & Hall, London.
Ji, Y., 2020. Shear-flow Characteristics of Rock Fractures and Implications for Injection-induced Seismicity. Nanyang Technological University.
Ji, Y., Wu, W., 2020. Injection-driven fracture instability in granite: mechanism and implications. Tectonophysics 791, 228572.
Ji, Y., Kluge, C., Hofmann, H., Blöcher, G., 2022. Effects of external temperature and dead volume on laboratory measurements of pore pressure and injected volume in a rock fracture. J. Rock Mech. Geotech. Eng. https://doi.org/10.1016/j.jrmge.2021.12.007.
Ji, Y., Wanniarachchi, W.A.M., Wu, W., 2020. Effect of fluid pressure heterogeneity on injection-induced fracture activation. Comput. Geotech. 123, 103589.
Ji, Y., Fang, Z., Wei, W., 2021a. Fluid overpressurization on rock fractures: experimental investigation and analytical modelling. Rock Mech. Rock. Eng. 54 (6), 3039–3050.
Ji, Y., Yoon, J.S., Zang, A., Wu, W., 2021b. Mitigation of injection-induced seismicity on undrained faults in granite using cyclic fluid injection. Int. J. Rock Mech. Min. Sci. 146, 104881.
Ji, Y., Yoon, J.S., Zang, A., Wu, W., 2021c. Shear stress transfer induced by fluid overpressurization and implications for injectioninduced fault activation in crystalline rocks. Rock Mech. Rock Eng. (Under review).
Ji, Y., Zhuang, L., Wu, W., Hofmann, H., Zang, A., Zimmermann, G., 2021d. Cyclic water injection potentially mitigates seismic risks by promoting slow and stable slip of a natural fracture in granite. Rock Mech. Rock. Eng. 1–17.
Jones, T.A., Detwiler, R.L., 2016. Fracture sealing by mineral precipitation: the role of small-scale mineral heterogeneity. Geophys. Res. Lett. 43 (14), 7564–7571.
KC, B., Ghazanfari, E., 2021. Geothermal reservoir stimulation through hydro-shearing: an experimental study under conditions close to enhanced geothermal systems. Geothermics 96, 102200.
Kilgore, B.D., Blanpied, M.L., Dieterich, J.H., 1993. Velocity dependent friction of granite over a wide range of conditions. Geophys. Res. Lett. 20 (10), 903–906.
Kilgore, B., Beeler, N., Lozos, J., Oglesby, D., 2017. Rock friction under variable normal stress. J. Geophys. Res. 122, 7042–7075.
Kim, K.-H., Ree, J.-H., Kim, Y., Kim, S., Kang, S.Y., Seo, W., 2018. Assessing whether the 2017 Mw 5.4 Pohang earthquake in South Korea was an induced event. Science 360 (6392), 1007–1009.
Kluge, C., Blöcher, G., Barnhoorn, A., Schmittbuhl, J., Bruhn, D., 2021. Permeability evolution during shear zone initiation in low-porosity rocks. Rock Mech. Rock. Eng. 54, 5221–5244.
Kohli, A.H., Zoback, M.D., 2013. Frictional properties of shale reservoir rocks. J. Geophys. Res. 118 (9), 5109–5125.
Kolawole, F., Johnston, C.S., Morgan, C.B., Chang, J.C., Marfurt, K.J., Lockner, D.A., Reches, Z., Carpenter, B.M., 2019. The susceptibility of Oklahoma's basement to seismic reactivation. Nat. Geosci. 12 (10), 839–844.
Labuz, J.F., Zang, A., 2012. Mohr–Coulomb failure criterion. Rock Mech. Rock. Eng. 45 (6), 975–979.
Lapusta, N., Barbot, S., 2012. Models of earthquakes and aseismic slip based on laboratory-derived rate-and-state friction laws. In: The Mechanics of Faulting: From Laboratory to Real Earthquakes, pp. 153–207. Research Signpost.
Lee, K.-K., Ellsworth, W.L., Giardini, D., Townend, J., Ge, S., Shimamoto, T., Yeo, I.-W., Kang, T.-S., Rhie, J., Sheen, D.-H., Chang, C., Woo, J.-U., Langenbruch, C., 2019. Managing injection-induced seismic risks. Science 364 (6442), 730–732.
Leeman, J.R., Saffer, D.M., Scuderi, M.M., Marone, C., 2016. Laboratory observations of slow earthquakes and the spectrum of tectonic fault slip modes. Nat. Commun. 7, 11104.
Leeman, J.R., Marone, C., Saffer, D.M., 2018. Frictional mechanics of slow earthquakes. J. Geophys. Res. 123 (9), 7931–7949.
Lei, X., Huang, D., Su, J., Jiang, G., Wang, X., Wang, H., Guo, X., Fu, H., 2017a. Fault reactivation and earthquakes with magnitudes of up to Mw4.7 induced by shale-gas hydraulic fracturing in Sichuan Basin, China. Sci. Rep. 7 (1), 7971.
Lei, X., Li, S., Liu, L., 2017b. Fracturing behaviors of unfavorably oriented faults investigated using an acoustic emission monitor. In: Advances in Acoustic Emission Technology. Springer, pp. 229–240.
Lei, X., Su, J., Wang, Z., 2020. Growing seismicity in the Sichuan Basin and its association with industrial activities. Sci. China Earth Sci. 63 (11), 1633–1660.
Li, L., Tan, J., Wood, D.A., Zhao, Z., Becker, D., Lyu, Q., Shu, B., Chen, H., 2019. A review of the current status of induced seismicity monitoring for hydraulic fracturing in unconventional tight oil and gas reservoirs. Fuel 242, 195–210.
Linker, M., Dieterich, J., 1992. Effects of variable normal stress on rock friction: observations and constitutive equations. J. Geophys. Res. 97 (B4), 4923–4940.
Lockner, D.A., Byerlee, J.D., 1993. How geometrical constraints contribute to the weakness of mature faults. Nature 363 (6426), 250–252.
Lucas, Y., Ngo, V.V., Clément, A., Fritz, B., Schäfer, G., 2020. Modelling acid stimulation in the enhanced geothermal system of Soultz-sous-Forêts (Alsace, France). Geothermics 85, 101772.
Ma, S., Shimamoto, T., Yao, L., Togo, T., Kitajima, H., 2014. A rotary-shear low to high-velocity friction apparatus in Beijing to study rock friction at plate to seismic slip rates. Earthq. Sci. 27 (5), 469–497.
Ma, J., Querci, L., Hattendorf, B., Saar, M.O., Kong, X.-Z., 2020. The effect of mineral dissolution on the effective stress law for permeability in a tight sandstone. Geophys. Res. Lett. 47 (15) (e2020GL088346).
Ma, J., Ahkami, M., Saar, M.O., Kong, X.-Z., 2021. Quantification of mineral accessible surface area and flow-dependent fluid-mineral reactivity at the pore scale. Chem. Geol. 563, 120042.
Mackwell, S.J., Paterson, M.S., 2002. New developments in deformation studies: high-strain deformation. Rev. Mineral. Geochem. 51 (1), 1–19.
Majer, E.L., Baria, R., Stark, M., Oates, S., Bommer, J., Smith, B., Asanuma, H., 2007. Induced seismicity associated with Enhanced Geothermal Systems. Geothermics 36 (3), 185–222.
Marone, C., 1998. Laboratory-derived friction laws and their application to seismic faulting. Annu. Rev. Earth Planet. Sci. 26 (1), 643–696.
Marone, C., Scholz, C., 1989. Particle-size distribution and microstructures within simulated fault gouge. J. Struct. Geol. 11 (7), 799–814.
McGarr, A., 2014. Maximum magnitude earthquakes induced by fluid injection. J. Geophys. Res. 119 (2), 1008–1019.
McGarr, A., Barbour, A.J., 2018. Injection-induced moment release can also be aseismic. Geophys. Res. Lett. 45, 5344–5351.
Nemoto, K., Moriya, H., Niitsuma, H., Tsuchiya, N., 2008. Mechanical and hydraulic coupling of injection-induced slip along pre-existing fractures. Geothermics 37 (2), 157–172.
Nicolas, A., Blöcher, G., Kluge, C., Li, Z., Hofmann, H., Pei, L., Milsch, H., Fortin, J., Guéguen, Y., 2020. Pore pressure pulse migration in microcracked andesite recorded with fibre optic sensors. Geomech. Energy Environ. 24.
Noël, C., Passelègue, F.X., Giorgetti, C., Violay, M., 2019. Fault reactivation during fluid pressure oscillations: transition from stable to unstable slip. J. Geophys. Res. 124, 10940–10953.
Nouailletas, O., Perlot, C., Rivard, P., Ballivy, G., La Borderie, C., 2017. Impact of acid attack on the shear behaviour of a carbonate rock joint. Rock Mech. Rock. Eng. 50, 1439–1451.
Okazaki, K., Katayama, I., Noda, H., 2013. Shear-induced permeability anisotropy of simulated serpentinite gouge produced by triaxial deformation experiments. Geophys. Res. Lett. 40 (7), 1290–1294.
Park, H., Osada, M., Matsushita, T., Takahashi, M., Ito, K., 2013. Development of coupled shear-flow-visualization apparatus and data analysis. Int. J. Rock Mech. Min. Sci. 63, 72–81.

Passelègue, F., Spagnuolo, E., Violay, M., Nielsen, S., Di Toro, G., Schubnel, A., 2016a. Frictional evolution, acoustic emissions activity, and off-fault damage in simulated faults sheared at seismic slip rates. J. Geophys. Res. 121 (10), 7490–7513.
Passelègue, F.X., Schubnel, A., Nielsen, S., Bhat, H.S., Deldicque, D., Madariaga, R., 2016b. Dynamic rupture processes inferred from laboratory microearthquakes. J. Geophys. Res. 121 (6), 4343–4365.
Passelègue, F.X., Brantut, N., Mitchell, T.M., 2018. Fault reactivation by fluid injection: Controls from stress state and injection rate. Geophys. Res. Lett. 45 (23), 12,837–12,846.
Passelègue, F.X., Almakari, M., Dublanchet, P., Barras, F., Fortin, J., Violay, M., 2020. Initial effective stress controls the nature of earthquakes. Nat. Commun. 11 (1), 5132.
Paterson, M.S., Wong, T.-f., 2005. Experimental Rock Deformation-The Brittle Field. Springer Science & Business Media.
Polak, A., Elsworth, D., Yasuhara, H., Grader, A.S., Halleck, P.M., 2003. Permeability reduction of a natural fracture under net dissolution by hydrothermal fluids. Geophys. Res. Lett. 30 (20).
Portier, S., Vuataz, F.-D., Nami, P., Sanjuan, B., Gérard, A., 2009. Chemical stimulation techniques for geothermal wells: experiments on the three-well EGS system at Soultz-sous-Forêts, France. Geothermics 38 (4), 349–359.
Proctor, B., Lockner, D.A., Kilgore, B.D., Mitchell, T.M., Beeler, N.M., 2020. Direct evidence for fluid pressure, dilatancy, and compaction affecting slip in isolated faults. Geophys. Res. Lett. 47 (e2019GL086767).
Rathnaweera, T.D., Wu, W., Ji, Y., Gamage, R.P., 2020. Understanding injection-induced seismicity in enhanced geothermal systems: from the coupled thermo-hydro-mechanical-chemical process to anthropogenic earthquake prediction. Earth Sci. Rev. 205, 103182.
Reinsch, T., Blöcher, G., Milsch, H., Bremer, K., Lewis, E., Leen, G., Lochmann, S., 2012. A fibre optic sensor for the in situ determination of rock physical properties. Int. J. Rock Mech. Min. Sci. 55, 55–62.
Rice, J.R., 2006. Heating and weakening of faults during earthquake slip. J. Geophys. Res. 111 (B5).
Ruina, A., 1983. Slip instability and state variable friction laws. J. Geophys. Res. 88 (B12), 10359–10370.
Rutter, E., Hackston, A., 2017. On the effective stress law for rock-on-rock frictional sliding, and fault slip triggered by means of fluid injection. Philos. Trans. A Math. Phys. Eng. Sci. 375 (2103), 20160001.
Samuelson, J., Spiers, C.J., 2012. Fault friction and slip stability not affected by CO_2 storage: evidence from short-term laboratory experiments on North Sea reservoir sandstones and caprocks. Int. J. Greenhouse Gas Control 11, S78–S90.
Rutter, E.H., Mecklenburgh, J., 2018. Influence of Normal and Shear Stress on the Hydraulic Transmissivity of Thin Cracks in a Tight Quartz Sandstone, a Granite, and a Shale. J. Geophys. Res. Solid Earth 123 (2), 1262–1285.
Samuelson, J., Elsworth, D., Marone, C., 2009. Shear-induced dilatancy of fluid-saturated faults: experiment and theory. J. Geophys. Res. 114 (B12).
Scholz, C.H., 1998. Earthquakes and friction laws. Nature 391 (6662), 37–42.
Scholz, C.H., 2019. The Mechanics of Earthquakes and Faulting. Cambridge University Press, Cambridge, United Kingdom.
Scholz, C., Engelder, J., 1976. The role of asperity indentation and ploughing in rock friction—I: asperity creep and stick-slip. Int. J. Rock Mech. Min. Sci. Geomech. Abstr. 13 (5), 149–154.
Scuderi, M.M., Collettini, C., 2016. The role of fluid pressure in induced vs. triggered seismicity: insights from rock deformation experiments on carbonates. Sci. Rep. 6 (1), 1–9.
Scuderi, M.M., Collettini, C., 2018. Fluid injection and the mechanics of frictional stability of shale-bearing faults. J. Geophys. Res. 123 (10), 8364–8384.
Scuderi, M.M., Carpenter, B.M., Marone, C., 2014. Physicochemical processes of frictional healing: effects of water on stick-slip stress drop and friction of granular fault gouge. J. Geophys. Res. 119 (5), 4090–4105.
Scuderi, M.M., Marone, C., Tinti, E., Di Stefano, G., Collettini, C., 2016. Precursory changes in seismic velocity for the spectrum of earthquake failure modes. Nat. Geosci. 9 (9), 695–700.
Scuderi, M.M., Collettini, C., Marone, C., 2017. Frictional stability and earthquake triggering during fluid pressure stimulation of an experimental fault. Earth Planet. Sci. Lett. 477, 84–96.
Shang, D., Zhao, Z., Dou, Z., Yang, Q., 2020. Shear behaviors of granite fractures immersed in chemical solutions. Eng. Geol. 279, 105869.
Shapiro, S.A., Krüger, O.S., Dinske, C., Langenbruch, C., 2011. Magnitudes of induced earthquakes and geometric scales of fluid-stimulated rock volumes. Geophysics 76 (6), WC55–WC63.
Shen, H., Zhang, Q., Li, Q., Li, X., Shi, L., Shen, N., 2020. Experimental and numerical investigations of the dynamic permeability evolution of a fracture in granite during shearing under different normal stress conditions. Rock Mech. Rock. Eng. 53 (10), 4429–4447.
Sheng, M., Li, P., Zhuang, X., Wang, J., 2020. Influence of cyclic normal stress on shear friction of EGS granite fractures. Eng. Fract. Mech. 238, 107268.
Shreedharan, S., Rivière, J., Bhattacharya, P., Marone, C., 2019. Frictional state evolution during normal stress perturbations probed with ultrasonic waves. J. Geophys. Res. 124, 5469–5491.
Sibson, R.H., 1986. Earthquakes and rock deformation in crustal fault zones. Annu. Rev. Earth Planet. Sci. 14 (1), 149–175.
Sibson, R.H., 1990. Rupture nucleation on unfavorably oriented faults. Bull. Seismol. Soc. Am. 80 (6A), 1580–1604.
Sibson, R., 1992. Implications of fault-valve behaviour for rupture nucleation and recurrence. Tectonophysics 211 (1-4), 283–293.
Sibson, R.H., 2000. Fluid involvement in normal faulting. J. Geodyn. 29 (3–5), 469–499.
Tembe, S., Lockner, D.A., Wong, T.-F., 2010. Effect of clay content and mineralogy on frictional sliding behavior of simulated gouges: Binary and ternary mixtures of quartz, illite, and montmorillonite. J. Geophys. Res. 115 (B3).
Tinti, E., Scuderi, M.M., Scognamiglio, L., Di Stefano, G., Marone, C., Collettini, C., 2016. On the evolution of elastic properties during laboratory stick-slip experiments spanning the transition from slow slip to dynamic rupture. J. Geophys. Res. 121 (12), 8569–8594.
Ujiie, K., Tsutsumi, A., 2010. High-velocity frictional properties of clay-rich fault gouge in a megasplay fault zone, Nankai subduction zone. Geophys. Res. Lett. 37 (24).
Walsh, F.R., Zoback, M.D., 2015. Oklahoma's recent earthquakes and saltwater disposal. Sci. Adv. 1 (5), e1500195.
Wang, J., Ge, H., Wang, X., Shen, Y., Liu, T., Zhang, Y., Meng, F., 2019. Effect of clay and organic matter content on the shear slip properties of shale. J. Geophys. Res. 124 (9), 9505–9525.
Wang, L., Kwiatek, G., Rybacki, E., Bohnhoff, M., Dresen, G., 2020a. Injection-induced seismic moment release and laboratory fault slip: implications for fluid-induced seismicity. Geophys. Res. Lett. 47 (22) (e2020GL089576).
Wang, L., Kwiatek, G., Rybacki, E., Bonnelye, A., Bohnhoff, M., Dresen, G., 2020b. Laboratory study on fluid-induced fault slip behavior: the role of fluid pressurization rate. Geophys. Res. Lett. 47 e2019GL086627).
Wibberley, C.A.J., 2002. Hydraulic diffusivity of fault gouge zones and implications for thermal pressurization during seismic slip. Earth, Planets Space 54 (11), 1153–1171.
Wibberley, C.A.J., Shimamoto, T., 2003. Internal structure and permeability of major strike-slip fault zones: the median Tectonic Line in Mie Prefecture, Southwest Japan. J. Struct. Geol. 25 (1), 59–78.
Wibberley, C.A., Shimamoto, T., 2005. Earthquake slip weakening and asperities explained by thermal pressurization. Nature 436 (7051), 689–692.
Wilson, M.P., Foulger, G.R., Gluyas, J.G., Davies, R.J., Julian, B.R., 2017. HiQuake: the human-induced earthquake database. Seismol. Res. Lett. 88 (6), 1560–1565.
Woo, J.U., Kim, M., Sheen, D.H., Kang, T.S., Rhie, J., Grigoli, F., Ellsworth, W.L., Giardini, D., 2019. An in-depth seismological analysis revealing a causal link between the 2017 Mw 5.5 Pohang earthquake and EGS project. J. Geophys. Res. 124, 13060–13078.
Xia, K., Rosakis, A.J., Kanamori, H., 2004. Laboratory earthquakes: the sub-rayleigh-to-supershear rupture transition. Science 303 (5665), 1859–1861.
Xia, K., Rosakis, A.J., Kanamori, H., Rice, J.R., 2005. Laboratory earthquakes along inhomogeneous faults: directionality and supershear. Science 308 (5722), 681–684.
Xing, T., Zhu, W., French, M., Belzer, B., 2019. Stabilizing effect of high pore fluid pressure on slip behaviors of gouge-bearing faults. J. Geophys. Res. 124 (9), 9526–9545.
Yao, L., Ma, S., Chen, J., Shimamoto, T., He, H., 2018. Flash heating and local fluid pressurization lead to rapid weakening in water-saturated fault gouges. J. Geophys. Res. 123 (10), 9084–9100.
Yarushina, V.M., Bercovici, D., 2013. Mineral carbon sequestration and induced seismicity. Geophys. Res. Lett. 40 (5), 814–818.
Yasuhara, H., Elsworth, D., Polak, A., 2004. Evolution of permeability in a natural fracture: significant role of pressure solution. J. Geophys. Res. 109 (B3).
Ye, Z., Ghassemi, A., 2018. Injection-induced shear slip and permeability enhancement in granite fractures. J. Geophys. Res. 123 (10), 9009–9032.
Ye, Z., Ghassemi, A., 2020. Heterogeneous fracture slip and aseismic-seismic transition in a triaxial injection test. Geophys. Res. Lett. 47 (14) https://doi.org/10.1029/2020GL087739.
Zang, A., Stephansson, O., 2009. Stress Field of the Earth's Crust. Springer Science & Business Media.
Zang, A., Yoon, J.S., Stephansson, O., Heidbach, O., 2013. Fatigue hydraulic fracturing by cyclic reservoir treatment enhances permeability and reduces induced seismicity. Geophys. J. Int. 195 (2), 1282–1287.
Zang, A., Oye, V., Jousset, P., Deichmann, N., Gritto, R., McGarr, A., Majer, E., Bruhn, D., 2014. Analysis of induced seismicity in geothermal reservoirs – an overview. Geothermics 52, 6–21.
Zang, A., Stephansson, O., Stenberg, L., Plenkers, K., Specht, S., Milkereit, C., Schill, E., Kwiatek, G., Dresen, G., Zimmermann, G., Dahm, T., Weber, M., 2017. Hydraulic fracture monitoring in hard rock at 410m depth with an advanced fluid-injection protocol and extensive sensor array. Geophys. J. Int. 208 (2), 790–813.
Zang, A., Zimmermann, G., Hofmann, H., Stephansson, O., Min, K.-B., Kim, K.Y., 2019. How to reduce fluid-injection-induced seismicity. Rock Mech. Rock. Eng. 52 (2), 475–493.
Zhang, W., Mehrabian, A., 2020a. Poroelastic solution for the nonlinear injectivity of subsurface rocks with strain-induced permeability variations. Water Resour. Res. 56 (8) (e2020WR027620).
Zhang, W., Mehrabian, A., 2020b. Poroelastic solution for the nonlinear productivity index of wells in stress-sensitive reservoir rocks. SPE J. 1–15.
Zhang, W., Mehrabian, A., 2021. Nonlinear and non-local analytical solution for Darcy–Forchheimer flow through a deformable porous inclusion within a semi-infinite elastic medium. J. Fluid Mech. 911, A49.

Zhang, Q., Li, X., Bai, B., Pei, L., Shi, L., Wang, Y., 2019. Development of a direct-shear apparatus coupling with high pore pressure and elevated temperatures. Rock Mech. Rock. Eng. 52 (9), 3475–3484.
Zhang, Q., Li, X., Bai, B., Hu, H., 2019b. The shear behavior of sandstone joints under different fluid and temperature conditions. Eng. Geol. 257, 105143.
Zhou, C., Wan, Z., Zhang, Y., Gu, B., 2018. Experimental study on hydraulic fracturing of granite under thermal shock. Geothermics 71, 146–155.
Zhuang, L., Zang, A., 2021. Laboratory hydraulic fracturing experiments on crystalline rock for geothermal purposes. Earth Sci. Rev. 216, 103580.
Zhuang, L., Kim, K.Y., Jung, S.G., Diaz, M., Min, K.-B., Zang, A., Stephansson, O., Zimmermann, G., Yoon, J.-S., Hofmann, H., 2019. Cyclic hydraulic fracturing of pocheon granite cores and its impact on breakdown pressure, acoustic emission amplitudes and injectivity. Int. J. Rock Mech. Min. Sci. 122, 104065.
Zhuang, L., Jung, S.G., Diaz, M., Kim, K.Y., Hofmann, H., Min, K.-B., Zang, A., Stephansson, O., Zimmermann, G., Yoon, J.-S., 2020. Laboratory true triaxial hydraulic fracturing of granite under six fluid injection schemes and grain-scale fracture observations. Rock Mech. Rock. Eng. 53, 4329–4344.
Zoback, M.D., 2010. Reservoir Geomechanics. Cambridge University Press, Cambridge, United Kingdom.